Chapter 4
Nanostructured α-Fe_2O_3 Photoanodes

Kevin Sivula

4.1 Introduction

Since the seminal demonstration of photocatalytic hydrogen production from water splitting with TiO_2 [1], scientists and engineers have sustained the search for a photoelectrochemical (PEC) water-splitting material combining efficient solar light harvesting, high quantum efficiency, practical durability, and low cost. However to date, no single semiconducting material which meets all of these requirements has been found [2]. While systems delivering high solar-to-hydrogen (STH) efficiency have been demonstrated using III–V semiconductor materials with optimized band gaps and energy levels straddling the hydrogen and oxygen redox potentials their cost and stability are a major disadvantage [3]. In contrast, many transition metal oxide semiconductors offer suitable stability to the chemically harsh environment of water, oxygen, and light inherent to PEC water splitting. For example, TiO_2 and WO_3 have been thoroughly investigated and optimized to deliver high single-wavelength quantum efficiencies [4, 5]. Unfortunately the stability of these oxides in aqueous environments, aided by an energetically low valence band which is defined largely by O 2p energy levels, also brings a large bandgap which renders these materials transparent to most of the incident solar illumination. This limits the maximum possible STH conversion efficiency. Specifically, considering the bandgap energies, E_g, alone, TiO_2 (anatase, $E_g = 3.2$ eV) and WO_3 ($E_g = 2.6$ eV) could only convert 3.4 and 10.2%, respectively, of the sun's energy into hydrogen. A more accurate evaluation of the potential efficiencies, including expected kinetic losses, suggests that only 5% STH is possible with WO_3 [6].

In addition to sufficient light absorption and stability, a semiconducting material used for PEC water splitting must be made from raw materials with ample availability

K. Sivula (✉)
Institut des sciences et ingénierie chimiques, Ecole Polytechnique Fédérale de Lausanne, CH-1015 Lausanne, Switzerland
e-mail: kevin.sivula@epfl.ch

R. van de Krol and M. Grätzel (eds.), *Photoelectrochemical Hydrogen Production*, Electronic Materials: Science & Technology 102, DOI 10.1007/978-1-4614-1380-6_4,

to be relevant for energy conversion on a global scale. Iron(III) oxide is a promising material in light of these requirements. With a potential to convert 16.8% of the sun's energy into hydrogen [6], it has been extensively examined for application to solar water splitting. In this chapter the advantageous properties of Fe_2O_3 as well as the challenges it presents are examined in the context of PEC water splitting. The most recent efforts at improving photon harvesting by nanostructuring are reviewed, and continuing efforts to control the surface catalysis, and enhance the electronic properties by doping, are also addressed by examining recent literature reports in the field.

4.2 Iron(III) Oxide: A Promising Material for Solar Hydrogen Production

As iron is a readily oxidized metal, and iron ions can exist in different charge states (mainly 2+ and 3+) separated by relatively small energy differences, there are many forms of iron oxide both found in nature and that can be synthesized easily in the lab. In addition, because iron is a common element in the earth's crust (6.3% by weight) iron oxide is everywhere around us, giving, for example, the geological formations of the southwest USA their brown-red color. Commonly (and perhaps unfortunately), iron oxide is better known as a nuisance material, and by its common name – rust – the red-brown corrosion product of iron in the presence of oxygen and moisture. However, its chromatic characteristics also imply the ability to absorb solar irradiation. This coupled with its abundance and nontoxicity make iron oxide a particularly attractive material for use in solar energy conversion. The distinct properties of all of the iron oxides are comprehensively presented in a recent book by Cornell and Schwertmann [7]. Here, a brief summary is presented of the important and unique properties of iron(III) oxide, α-Fe_2O_3, or hematite, the most frequent iron oxide employed for solar hydrogen production. These properties highlight both the promising aspects and the challenges that hematite presents as a material for solar energy conversion.

4.2.1 Structural and Material Properties

For iron oxide in its fully oxidized form, each iron atom is in the +3 oxidation state. There are thus two O^{2-} anions for every three Fe^{3+}. Even considering this stoichiometry, there are many types of Fe_2O_3 including amorphous structures. The α (hematite) and γ (maghemite) forms are two most common crystalline structures found in nature. Maghemite can be considered to be a form of magnetite (Fe_3O_4), a ferrimagnetic spinel iron(II–III) oxide, with cation vacancies. Indeed, natural maghemite arrives from the oxidation of magnetite, and retains strong (ferri) magnetic properties. While this form of iron oxide has found wide-spread use as

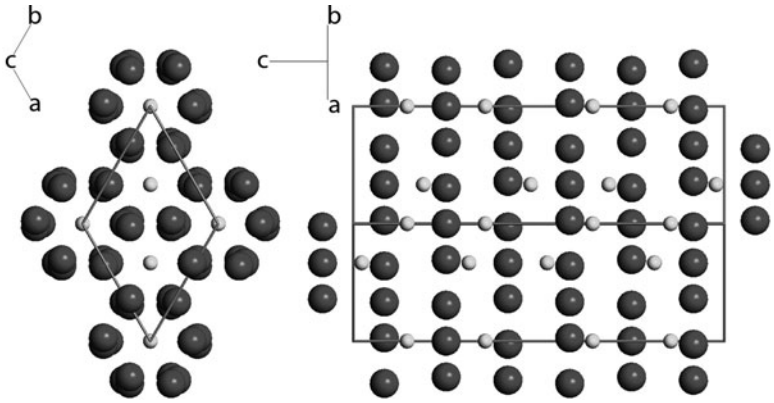

Fig. 4.1 The crystal structure of hematite as seen looking down the [001] direction (*left*) and the [8] direction (*right*). Oxygen anions are *dark gray* and iron cations are *light gray*. The unit cell is outlined, and the orientation map is shown for each view

a magnetic recording medium (giving floppy disks and cassette tapes their brown color) the physical properties have not been found to be suitable for photoelectrochemistry. In addition, maghemite, as with all of the other iron oxides converts to hematite, the most thermodynamically stable form of iron oxide (under standard conditions) upon treatment with heat.

Hematite, alpha-Fe_2O_3, is the most common form of iron oxide. Due to its prevalence, hardness (6.5 on Mohs scale), and chemical and thermal stability (decomposition temperature of 1,566°C), it has found historic use as a polishing powder known as jeweler's rouge. In addition, its ability to absorb light has made it an attractive choice for pigments in paints and even cosmetics. Alpha-Fe_2O_3 has the same crystal structure of corundum, Al_2O_3, which is trigonal (hexagonal scalenohedral, symbol $\bar{3}$ 2/m) with space group $R\bar{3}c$ with lattice parameters $a = 5.0356$ Å, $c = 13.7489$ Å, and six formula units per unit cell [7]. It is easy to understand hematite's structure based on the packing of the anions, O^{2-}, which are arranged in a hexagonal closed-packed lattice along the [001] direction. The cations, Fe^{3+}, occupy the two-thirds of the octahedral interstices (regularly, with two filled followed by one vacant) in the (001) basal planes. The tetrahedral sites remain unoccupied. Two views of the hematite crystal structure are shown in Fig. 4.1. Here the layered structure of iron oxide is evident; layers of closed-packed oxygen anions alternate with iron cations bilayers in the [001] direction. The arrangement of cations can also be thought of producing pairs of FeO_6^{9-} octahedra which share edges with three neighboring octahedra in the same plane and one face with an octahedron in an adjacent plane in the [001] direction. This face sharing is responsible for a trigonal distortion of the octahedron. In the FeO_6^{9-} octahedra which share faces, iron atoms are repelled along the direction normal to the [001] axis. Consequently, the O–O distance in shared faces is shorter than in an unshared face. However, the electronic structures of these distorted FeO_6^{9-} octahedral are quite similar to undistorted clusters [7].

4.2.2 Magnetic Properties

The arrangement of the oxygen anions and the high-spin (d^5 configuration) iron cations in iron(III) oxide naturally affects the orientation of the iron atoms' spin magnetic moment and thus the observed bulk magnetic properties. The diverse magnetic properties of all the iron(III) oxides have been recently reviewed [9]. In brief, the inverse spinel structure of maghemite (γ-Fe_2O_3) results in the presence of two interpenetrating sublattices and gives rise to ferrimagnetic behavior and high susceptibilities. In contrast, hematite is antiferromagnetic (temperatures below 260 K) or a weak (parasitic) ferromagnet at room temperature. The latter is due to the ferromagnetic coupling of the spins within the (001) basal (iron bilayer) planes and antiferromagnetic coupling between iron bilayers along the [001] direction [10]. Here the trigonal distortion of the FeO_6^{9-} octahedra causes the spins to become slightly canted (about 5°) causing the destabilization of their perfectly antiparallel arrangement (parasitic ferromagnetism). Above the Néel temperature (950 K), the iron spins become thermally disordered and a paramagnetic material results [9]. While the magnetic properties of hematite are not particularly pertinent to its photoelectrochemical performance, the iron spin configuration does influence the optoelectronic and carrier transport properties of hematite. In addition, exploiting magnetic characteristics with Mössbauer spectroscopy to identify phases in iron oxides prepared for electrochemical application has proven to be a useful technique [11–13].

4.2.3 Optoelectronic Characteristics

The dense (hexagonal close) packing of oxygen combined with the interstitially positioned iron yields a very dense structure (5.26 g/cm^3) exhibiting a high polarizability and a high refractive index (3.15) [14]. This layered structure also generates complex behavior when interacting with photons and electrons. These attributes of hematite should be properly understood for application as a semiconductor for solar water splitting. Decades of research have passed scrutinizing the mechanisms of charge transport and light absorption, and while hematite is still not completely understood, much progress has been made.

The absorption of photons by hematite is shown in Fig. 4.2 (left side) and begins in the near infrared spectral region. This initial weak absorption is due to d–d transition states between electron energy levels of the d^5 Fe^{3+} ion, which are split by an intrinsic crystal field [16]. Two absorption bands in this spectral region centered around $\lambda = 860$ and 640 nm with absorption coefficients, α, of the order 10^3 cm^{-1} have been accurately assigned using ligand field theory to spin-forbidden transitions from $^6A_{1g}$ to $^4T_{1g}$ and $^4T_{2g}$, respectively [15, 16]. While photoexcitation of hematite at these wavelengths has been shown to increase its conductivity [15], sustained photocurrent is not observed in a PEC system (see Sect. 4.2.4) upon

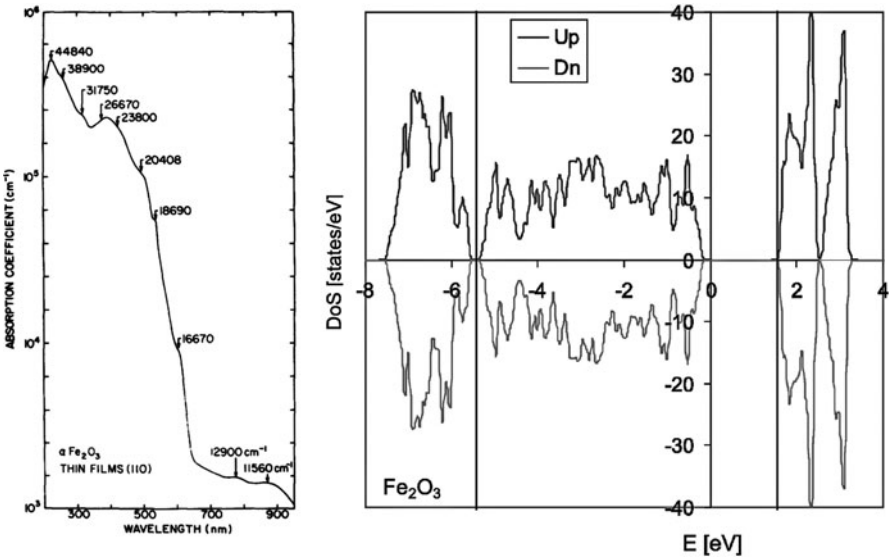

Fig. 4.2 Optical and electronic properties of hematite: The left graph shows the absorption coefficient as a function of photon wavelength in hematite thin films prepared by r.f. sputtering (from [15] used with permission). The *right graph* shows the calculated density of electron states (spin up and down) in hematite. The Fermi energy is at 0 eV and two lines at about −5.5 and 1.8 eV divide the plot into three regions: the lowest energy region contains the occupied Fe-d states; the next energy region contains the occupied O-p states; the region above the gap contains the empty Fe-d levels (Reprinted figure with permission from Velev, J., Bandyopadhyay, A., Butler, W.H., Sarker, S.: Phys. Rev. B: Condens. Matter **71**, 205–208 (2005). Copyright 2005 by the American Physical Society)

irradiation below the bandgap energy, E_g (which, depending on the method of preparation of hematite, is usually reported to be between 1.9 and 2.2 eV or 650–560 nm [14]). The absorption coefficient of pure hematite increases abruptly at the band gap energy and further up the electromagnetic spectrum α continues to increase with additional absorption peaks having been observed centered on 2.4, 3.2, and 5.8 eV (with α on the order of 10^5 cm^{-1}) in samples of polycrystalline hematite [17]. Hematite's strong absorption of yellow to ultraviolet photons in the visible region and transmission of orange to infrared photons gives it a characteristic red color. However, it is fairly uniform reflectivity as a function of visible light wavelength gives polished bulk samples of hematite a metallic look.

Since the electronic nature of the band gap in hematite is of great interest to understand its performance as a material for solar energy conversion, much work has focused on this aspect. Tauc analysis of the bandgap absorption onset, which assumes that the energy state bands are parabolic with respect to the crystal momentum, most frequently indicates an indirect (phonon-assisted) band gap transition [18]. However, a few recent reports of a direct band gap in hematite have been attributed to quantum size-effects [19, 20]. The initial orbital

assignments of the bandgap suggested it was due to an indirect transition of Fe^{3+} d–d origin [15, 21], and that a stronger direct transition involving a charge transfer from an O 2p orbital to Fe 3d did not occur until 3.2 eV [21]. This led to a hypothesis that two different types of p-type charge carriers (holes) could be produced in hematite, depending on the excitation mechanism, and were responsive for the observed difference in PEC performance as a function of wavelength [22, 23]. However, the most recent ab initio calculations to determine the electronic structure of hematite by the Hartree–Fock approach [24] and density functional theory with a local spin-density approximation and coulomb correlation [25, 26] both predict that the highest occupied energy states are primarily O p in character and the lowest unoccupied states are from an empty Fe-d band (see Fig. 4.2, right). This conclusion is also supported by soft-X-ray (O *K*-edge) absorption and emission spectroscopy, which when compared to photoemission spectra from configuration-interaction FeO_6 cluster calculations, confirm that the valence band is at least strongly hybridized and indicates further that it is mostly of O 2p character [27]. These latest results not only suggest that pure stoichiometric hematite is a charge transfer insulator, and not a Mott–Hubbard type insulator – a detail that affects conduction models – but also contradicts the suggestion that two types of holes, originating from different transitions, could cause different PEC behavior.

Finally, as discussed in the next section, much effort has been placed on doping hematite with various elements to increase charge carrier conduction. These elements are typically present at 1 atom% or less, and while substitutional transition metal impurities have been predicted to introduce interband gap energy states [25], the same dopants have not been reported to significantly change the bandgap absorption energy or the absorption coefficient [28–31].

4.2.4 Charge Carrier Transport and Dynamics

During an electromagnetic energy absorption event in hematite, a photon with energy greater than the bandgap will excite an electron from an occupied to an unoccupied state. For this process to be useful for water splitting the excited electron and remaining electron vacancy (hole) must spatially separate and live long enough to reach points of their collection or reaction. Luminescence studies on nanoparticles show that the excitation of hematite with photons of 3.2 eV results in fluorescence quantum yields of about 1×10^{-5} [32]. This extremely low value of radiative carrier recombination suggests that fast nonradiative processes such as carrier trapping and phonon coupling are limiting the excited state lifetime [33]. Indeed, the ultra fast dynamics of excited states in hematite have been studied in nanoparticles, thin films, and single crystals using femtosecond laser spectroscopy [32, 33]. In nanoparticles it was found that the excited state decay profiles were independent of the pump power and the probe wavelength, and were not affected by lattice doping or surface modification. However, the lifetime of the excited state was determined to be very short – 70% of the transient absorption had disappeared

after just 8 ps and could not be detected after 100 ps [32]. Studies on epitaxially grown thin films (100 nm using an oxygen plasma-assisted molecular beam) reduced the influence of defect states in the bulk or on the surface compared to the nanoparticle case, but found similar excited state dynamics, which were described by the following scenario: Initially, hot electrons relax to the conduction band edge within 300 fs. Then their recombination with holes and trap states occurs within 3 ps. The resulting trap states can exist for hundreds of picoseconds or longer [33]. In addition, the dominant carrier trapping mechanism was ascribed to mid-gap Fe^{3+} d–d states. These carrier trap states have been reported to be 0.5–0.7 eV below the conduction band edge giving them an optical transition of about 1.5 eV [34, 35] and are thus likely the same spin-forbidden transitions intrinsic to hematite which were discussed in the previous section.

A common metric sought by researchers in the field of semiconductor solar energy conversion is the excited carrier diffusion length which describes how far an average excited state can travel before recombination, and is estimated by taking the square root of the product of the carrier lifetime and the diffusion coefficient. Thus an ultra short lifetime alone does not prevent high efficiency in a semiconductor for PEC energy conversion if the carriers have a high mobility through the crystal lattice. Accordingly, understanding the transport of carriers in hematite is equally important to understanding the lifetime.

The earliest work by Morin on pure sintered polycrystalline hematite describes very low electrical conductivities (ca. 10^{-14} Ω^{-1} cm^{-1}) [36], conduction electron concentrations of 10^{18} cm^{-3} at 1,000 K, and an activation-energy type electron mobility on the order of 10^{-2} $cm^2/V/s$ [37]. Studies on pure single crystals showed conductivities below 10^{-6} Ω^{-1} cm^{-1} and were not suitable for further electronic characterization [31]. These unusually small values obliged electrical conduction to be explained by Fe^{3+}/Fe^{2+} valence alternation on spatially localized 3d orbitals. Modeling studies have had success matching empirical data by describing the conduction mechanism with a small polaron model which includes the effect of the larger size of the Fe^{2+} ion and the associated lattice distortion (polaron) [38, 39]. Conduction of electrons or holes can then be best described by hopping of polarons with an activation energy. This conduction mechanism causes the mobility of carriers to increase with increased temperature, as transport is assisted by lattice vibrations [40]. The localized electron, small polaron model has also been further supported by experimental results including pulse radiolysis [41] and the previously mentioned femtosecond laser spectroscopy on nanoparticles [32].

Further studies of hematite single crystals identified a highly anisotropic electron transport with conduction within the iron bilayer (001) basal plane four orders of magnitude greater than perpendicular directions (parallel to [001]) [42, 43]. This discrepancy cannot be explained by the proximity of iron cations alone, as the shortest Fe–Fe distances are actually along the [001] direction and nevertheless they are quite similar to Fe–Fe distances in the basal planes [44]. However, the anisotropic conductivity can be classically explained considering Hund's rule and the magnetic structure of hematite. The ferromagnetic coupling of the spins in the (001) basal planes and antiferromagnetic coupling along the [001] direction create

an environment where electrons can move (n-type conductivity) within the iron bilayers (an environment of parallel spins) but are forbidden to hop across the oxygen plans to an iron bilayer with the opposite spins. Thus conduction in the [001] direction could only involve the movement of holes in the form of $Fe^{3+} \rightarrow Fe^{4+}$ electron transfer (p-type conductivity). This process is significantly slower in hematite [40]. While this classical explanation is generally accepted, recent ab initio electronic structure calculations combined with electron transfer (Marcus) theory have correctly predicted the large transport anisotropy in hematite but suggested it arises from the slowness of both hole and electron mobility across basal oxygen planes [10]. This is contrast to the classical conception as it does not consider electron transport to be forbidden in the [001] direction, but instead identifies the most important factor that influences the carrier mobility to be the electronic coupling – a quantity found to depend on both a superexchange interaction between the bridging oxygen atoms and the d-shell electron spin coupling.

Regardless of the specific details of the conduction mechanism it is clear that the conduction properties of pure hematite are not appropriate for use as a PEC semiconducting material. However, the conductive properties of hematite can be significantly enhanced by adding impurities to act as electronic dopants. Indeed, it is possible to increase conductivities and obtain both p-type and n-type alpha-Fe_2O_3 by doping with atoms such as (but not limited to) Mg^{2+}, Cu^{2+} (p-type) or with Ti^{4+}, Sn^{4+}, Zr^{4+}, Nb^{5+} (n-type) [40]. This behavior can be easily explained if we consider hematite to be a small polaron conductor with n- and p-type charge carriers assumed to be Fe^{2+} and Fe^{4+}, respectively. Then, if the impurity atoms substitute for a Fe^{3+} ion in the crystal lattice, they would cause the creation of Fe^{2+} (n-type) or Fe^{4+} (p-type) to balance the lattice charge. By doping at sufficient levels, high carrier conductivities can be attained. For example, Zr^{4+} was doped into single crystals to give donor densities on the order of 10^{19} cm^{-3}, conductivities around 0.1 Ω^{-1} cm^{-1} , and increased electron mobility (perhaps due to a increase in dielectric constant) of 0.1 $cm^2/V/s$ [31]. A review by Shinar and Kennedy outlines the dopants used for n-type iron oxide and their affect on electronic and PEC properties [45].

In addition to foreign impurities acting as electronic dopants, oxygen vacancies play an important role in the electronic behavior of hematite, and are the most commonly present intrinsic defects found in hematite [17]. In fact, samples of natural specular hematite have been found to be degenerate semiconductors due to oxygen deficiencies [34]. This is because oxygen vacancies act as n-type dopants by creating Fe^{2+} ions. Elevated temperature treatment (above 800°C) in air or anaerobic environments has been shown to create oxygen vacancies in hematite [17]. In this case, the oxygen vacancies may result in the formation of a Fe_3O_4 on the surface, distorting conduction measurements [38], and causing extensive recombination of carriers and reduced photoconduction that can be regained by oxygen treatment [46].

Finally, based on the lifetime and charge carrier mobility found in hematite, the diffusion length of excited carriers is expected to be small. Kennedy and Frese calculated the diffusion length for holes in n-type (Ti^{4+} doped) polycrystalline samples using the experimental photocurrent efficiency and a band-bending

semiconductor liquid interface model to determine the mean diffusion length for holes, L_p, outside the space charge region as 2–4 nm [18], and a similarly indirect method gave the same order of magnitude for pure Fe_2O_3 [47]. It is important to note that this value is significantly smaller compared to other oxides used for PEC water splitting. For example, values of L_p up to 10^4 and 150 nm have been reported for TiO_2 [48] and WO_3 [49], respectively. The ramifications of such a low value for L_p on the performance of hematite for PEC water splitting are discussed in the next section.

4.2.5 *Photoelectrochemical Properties: Challenges for Solar Water Oxidation*

Hardee and Bard [50] first turned to Fe_2O_3 as a material for water photolysis in 1976 seeking a photoanode material that was both stable under anodic polarization and capable of absorbing light with wavelengths longer than 400 nm. Before this, materials like GaAs, CdS, and Si had been found to absorb an appreciable amount of solar irradiation, but also to be unstable in aqueous environments under anodic condition. In contrast, materials like TiO_2, $SrTiO_3$, and SnO_2 had been identified as stable, but had bandgaps over 3 eV. Hardee and Bard made thin films of Fe_2O_3 on Ti and Pt substrates by chemical vapor deposition (CVD) of $Fe(AcAc)_3$ and observed photocurrent from their electrodes under illumination of 500 nm light at a potential of 0.8 V vs. SCE in 0.5 M KCl as electrolyte. Soon after Yeh and Hackerman [51] simply heated iron foils in air to make n-type iron oxide electrodes that gave photocurrents with no observable corrosion problems from pH 4.0 to 14 and Quinn et al. [52] showed that the (012) face of flux grown single crystals had collection efficiencies of around 20% at 0.5 V vs. SCE in 2 M NaOH (1.57 V vs. RHE) with 475 nm light. Further work by Kennedy et al. showed that p-type doping (with Pb^{2+} and Ca^{2+}) produced electrodes with high resistivity, but Si^{4+}, Sn^{4+}, and Ge^{4+} doped n-type hematite performed better than Ti^{4+}-doped hematite [28]. In addition, these initial studies showed that hematite had a flatband potential, V_{fb}, too low in energy to reduce water, and an external bias had to be applied to complete the water-splitting reaction (the electron energy scheme for a n-type hematite photoanode water-splitting system is shown in Fig. 4.3, left). Despite this, hematite was still considered to be a promising n-type photoanode material for solar water splitting due to its capability to absorb a significant portion of solar irradiation (29% of AM 1.0 [52]) and superior stability. Over the next decade numerous reports were published describing continuing studies with pure and doped Fe_2O_3 made by various routes. Notable extensive PEC studies were performed on Ti-doped polycrystalline-sintered hematite pellets [18, 23], and Nb-doped single crystals [53] – the latter reporting champion performance with an incident photon conversion efficiency (IPCE) of about 37% at 370 nm and 1.23 V vs. RHE in 1 M NaOH (27% at 1.06 V, see Fig. 4.3, right).

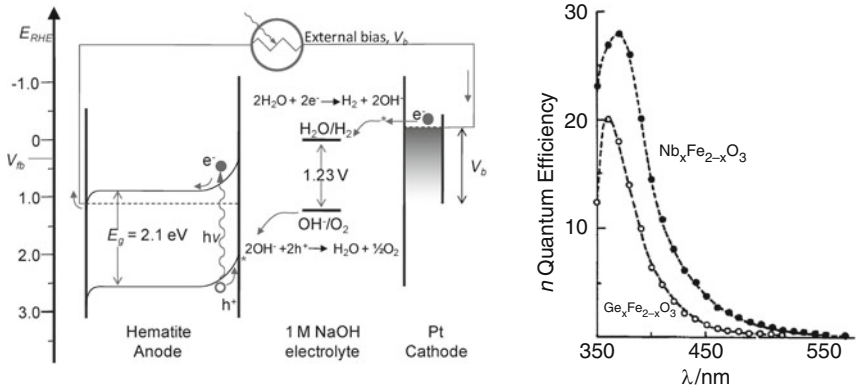

Fig. 4.3 Challenges presented by hematite: at left is an energy diagram showing a typical value of the flatband potential, V_{fb}, of n-type hematite, and the PEC water-splitting operation of a hematite photoanode under illumination and with an applied external bias, V_b. The right graph (from [53], with permission) shows the quantum efficiency vs. wavelength for Nb-doped and Ge-doped hematite single crystals at 0 V vs. SCE in 1 M NaOH (1.06 V vs. RHE). The efficiency is expressed in units of percent

A good review of these seminal studies on hematite has been given by Lindgren et al. [14] and in summary, the first decade of work identified the many challenges of employing this material for PEC water splitting:

1. Flatband potential too low in energy for water reduction [23, 52]
2. Large overpotential and slow water oxidation kinetics [23]
3. Low absorption coefficient, requiring relatively thick films [54, 55]
4. Poor majority carrier conductivity [35, 53]
5. Short diffusion length of minority carriers [18]

These limitations deterred much further interest in using hematite as a photoanode for water oxidation, as it appeared that the conversion of solar energy with high efficiency with it was not possible. Specifically, the small polaron transport and the deep inter-bandgap traps in hematite, which were discussed in Sect. 4.2.3, result in challenge numbers 4 and 5 above. Drawback 4 requires high doping levels to increase the ionized donor concentration and thus the conductivity. This in turn reduces the width of the space charge layer [56]. For example, donor dopant concentrations in the champion Nb-doped single crystals were found to be 5×10^{19} cm^{-3} by Mott–Schottky analysis [53]. Assuming classical depletion layer theory [56], this would result in a depletion layer width, W, of 7 nm at a band bending of 0.25 V and $\varepsilon = 100$. The low absorption coefficient in hematite (challenge 3) then implies that most of the incident photons will not be absorbed in the space charge region if the geometry of the photoanode is planar because the absorption depth (defined as α^{-1} = depth at which 63% of the photons are absorbed according to the Beer–Lambert law) for hematite ranges from 120 to 46 nm for photon wavelengths from 550 to 450 nm [17]. This would not be problematic if the diffusion length of the minority carriers was large

compared to the absorption depth, but it is only 2–4 nm (challenge 5). The effect of these limitations emerges as low quantum efficiencies, especially for the longer wavelengths. This is shown in Fig. 4.3 (right) with the highly efficient Nb-doped single crystals [53]. Even though peak quantum efficiency is close to 30% at $\lambda =$ 370 nm, it drops to below 5% at 450 nm and even though all of the incident irradiation is absorbed at 550 nm in the 0.1-mm thick films used, the quantum efficiency is less than 1%.

The above challenges and limitations suggest that the standard planar single crystal or sintered disk electrode geometries are not suitable for hematite, and indeed recent efforts with hematite have shown that challenges 3–5 can be overcome by optimizing the electrode morphology. These recent and exciting advances in hematite structuring are described in detail in the next section. In addition, the renewed efforts with structuring hematite have instigated further research to overcome challenges 1 and 2 listed above. These efforts are reviewed in Sect. 4.4.

4.3 Morphology Control of Fe_2O_3

Both the small (ca. 10 nm) space charge layer present in highly doped hematite (resulting from the necessity for conductivity) and the short (ca. 4 nm) diffusion length of minority carriers discussed in the previous section suggest that the ideal morphology of a hematite photoanode would be one where all of the hematite is within 10–20 nm of the semiconductor/liquid junction (SCLJ). This would give photogenerated holes a high probability of arriving at the SCLJ to oxidize water. Of course, one could simply deposit a 10 nm layer of hematite on a transparent substrate using a traditional deposition method. Then the poor absorptivity of such a film could be overcome by stacking multiple films in tandem. Indeed, this solution was first proposed by Itoh and Bockris in 1984 [55]. While this could fundamentally resolve the issue, it is cumbersome and expensive to implement, and in practice the thin iron oxide films were found to have poor performance due to the increased recombination of the photogenerated holes [54]. Fortunately, the recent development of tools to control the dimensions and morphology of materials at the nanometer length scale has offered more practical morphological solutions for hematite. Of course, the application of nanostructuring techniques to PEC solar hydrogen production has included more materials than simply hematite, with materials including WO_3 and TiO_2 also seeing noteworthy development. Two recent review articles from the research groups of both Augustynski [57] and Van de Krol [58] present a general overview of this topic. Currently, using new nanostructuring techniques, research groups are designing hematite with the proper morphology, feature size and dopants in order to enhance its ability to split water from solar irradiation. This section examines how directing the nanostructure of hematite has led to significant advances in its use as a material for photoelectrochemcial water splitting. This is done by analyzing how different deposition techniques have allowed the morphology control of hematite and affected its performance as a photoanode.

4.3.1 Colloidal Hematite

The nanoscopic manipulation of hematite was first mastered by Matijević's group in the early 1980s [59]. They created well-defined hematite colloidal particles through a hydothermal route and demonstrated morphological control by changing the concentration and the oxidative environment present during nucleation and growth. Spheres, disks, and plates of hematite were observed with lengths in the 100 nm range. However, no photochemistry was investigated with materials of this type until Moser and Grätzel reported halide photooxidation with colloidal dispersions of α-Fe_2O_3 2 years later [60]. In this work, 60 nm particles dispersed in aqueous solution were irradiated with 347 nm laser light and the extremely rapid (~10 ns) formation of I_2^- from iodide at high quantum efficiency (>80%) was observed. This result suggested an advantage of employing nanosized hematite where a larger fraction of the photogenerated carriers are produced closer to the surface as compared to the single crystal hematite or sintered pellets which had been reported at the time. Similar studies following shortly thereafter used various electron relays (*e.g.,* methyl viologen) and hole scavengers (e.g., methanol) to investigate the ability of Fe_2O_3 colloids to produce hydrogen from water [61–63]. While the conversion efficiency remained quite low even in these sacrificial systems, the optimum particle size, balancing bulk recombination and light harvesting, was estimated to be 100 nm in this work [63].

To date there have been numerous reports investigating the photocatalytic properties of colloidal α-Fe_2O_3. Most recently, layered "nanoflowers" [64] and hollow nanoparticles [65] synthesized via a simple solvothermal approach have shown enhanced photocatalytic activities for the degradation of Rhodamine B and diethyl phthalate, respectively, due to their large surface area. While these studies can give insight to the relative catalytic activity of different structures, given the band edge energies of hematite and the sluggish oxygen evolution reaction (OER) kinetics, it is likely that Fe_2O_3 colloids will not find application for water splitting but remain at the degradation of organics. However, the continued development of the precise control over hematite nanoparticle shape and size, like that recently demonstrated by Hu and Yu [66], should allow access to ideal electrode morphologies in the future.

4.3.2 Porous Thin Films from Colloids

Even if hematite nanoparticle dispersions could split water efficiently, the problems of gas separation and the reverse reactions (hydrogen oxidation and oxygen reduction) occurring in the heterogeneous mixture would remain. A more practical approach to water splitting is arguably a PEC cell with the anode and cathode evolving oxygen and hydrogen separately. This configuration provides the challenge of creating hematite with large surface area-to-volume ratio on the surface of

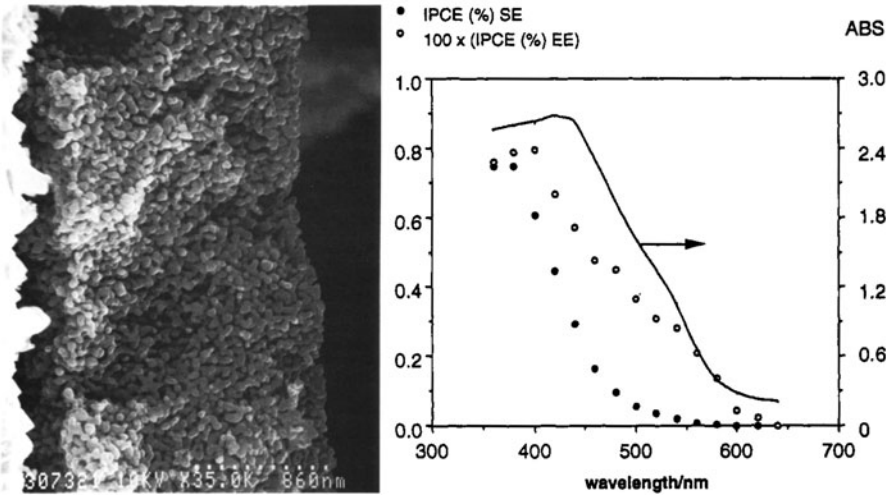

Fig. 4.4 Scanning electron micrograph (*left*) of the edge of a porous electrode made from sintered Fe_2O_3 sols on a conducting cassiterite (SnO_2) support (magnification 5,800 times). Absorption spectrum of the hematite electrode and quantum efficiency as a function of wavelength (*right*) obtained in 0.1 M NaOH at 1.4 V vs. RHE when illuminating the electrode through the substrate (SE) and directly onto the interface with the electrolyte (EE). Note that the scale of the IPCE values differs with a factor of 100 in the two cases. From [67] used with permission

a conducting support. The most straightforward way to create nanostructured photoelectrodes of hematite is to coat a sol onto an electrode and sinter to enforce interparticle connections – a method first perfected for solar energy conversion with TiO_2 in the dye-sensitized solar cell. This method was first attempted with hematite by Bjorksten et al. in 1994 [67]. Here, Fe_2O_3 sols created by the hydrolysis of $FeCl_3$ were concentrated and combined with surfactant before they were doctor-bladed onto transparent conducting oxide substrates (F-doped SnO_2) and sintered at 560°C. Micron-thick, porous thin films of necked hematite were observed to have good adhesion to the substrate and a primary particle size in the 25–75-nm range (see Fig. 4.4, left) However, the quantum efficiency (IPCE) of these photoanodes toward water splitting was quite low – on the order of 1% at 400 mV vs. SCE in 0.1 M NaOH (1.4 V vs. RHE) with 400 nm incident irradiation (see Fig. 4.4, right). The observations that the IPCE was 100 times lower when the anode was illuminated from the hematite/electrolyte interface as compared to the substrate/hematite interface and that the quantum efficiency did not improve significantly (only to 1.7%) when LiI was added as a hole scavenger led the authors to conclude that charge carrier recombination was the controlling factor for the photocurrent. The higher quantum efficiency of similar particles when dispersed in electrolyte [60] pointed to grain boundaries between the particles to be the cause of the recombination and poor performance. This limitation was addressed by Qain et al. [68] by altering the film thickness to optimize the light absorption/carrier transport issue. However, no significant improvement was obtained. Cathodic spikes observed during transient

measurements in this work suggested that no space charge layer was present, and that electron recombination at the hematite/electrolyte interface was also an important limitation.

Recent work on Fe_2O_3 films prepared by colloidal methods has identified a possible application of sensing organics in gas streams due to a change in electrical resistivity [69, 70] and suggested that the inclusion of metal nanoparticles [71, 72] or the presence of a spinel phase (γ-Fe_2O_3) [73] may increase the catalytic activity of these electrodes. However, a fundamental issue of particle size recognized in the seminal work [67] has yet been unresolved: Despite attempts to use particle sizes commensurate with the hole diffusion length (<10 nm), the temperatures required to sinter and make the films photoelectrochemically active result in primary particle sized too large to expect high photocurrents. Incorporating dopant atoms [74] and controlling feature size with templating techniques [75, 76] may result in an increase in performance for hematite films prepared by this inexpensive and scalable technique.

4.3.3 *Fe_2O_3 Nanowire Arrays*

An elegant solution to the problem of grain boundaries in hematite films created from the colloidal approach is to use nanosized rod or wire arrays. An array of single crystalline nanorods with diameters in the 10-nm range, attached and oriented orthogonally to the conducting substrate would eliminate grain boundaries, enhancing conduction to the substrate while still allowing photoproduced holes to efficiently reach the semiconductor/electrolyte interface. A simple method to create hematite arrays on a variety of substrates via a metastable akaganeite phase produced from the controlled precipitation of Fe(III) in aqueous solution was first reported by Vayssieres et al. [77], and investigated for water photoelectrolysis soon after [19]. Bundles of individual 5 nm nanorods with an average diameter of 50 nm and a length of 0.1–1.5 μm were investigated in perpendicular and parallel orientations to the substrate (Fig. 4.5, left). While the authors were able to show a small improvement when controlling the orientation (5% IPCE at 360 nm for the perpendicular nanorods vs. 3% for the parallel) the overall photocurrents remained low under white light illumination, even with hole scavenging iodide present. The large difference between the electrode performance when illuminating from different sides of the semitransparent photoanode observed in this work [79], and a recent report [80] examining the surface photovoltage on electrodes prepared the same way, suggest that bulk defects and the slow oxygen evolution kinetics of hematite are the major factors limiting the performance of this system.

Despite the poor performance of the nanowire arrays prepared by this technique it remains an intriguing morphology for hematite photoanodes. Another facile method to produce hematite nanowires by the simple thermal oxidation of iron foils has been reported by many groups [78, 81–84]. Due to the increased volume of the oxide over the metal, when foils of iron are thermally oxidized under the right

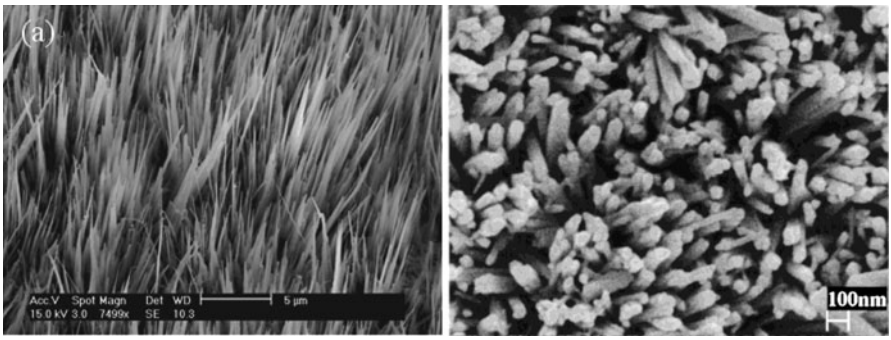

Fig. 4.5 Examples of hematite nanowire morphologies: SEM images of hematite prepared by the thermal oxidation method (*left*) from [78] and aqueous method (*right*) from [77] used with permission

conditions, arrays of Fe_2O_3 nanowires spontaneously grow from the surface of the iron. With diameters of 20–40 nm and lengths of up to 5 μm (see Fig. 4.5, right) these nanowire arrays would have large surface area, sufficient light absorption and a direct path for the conduction of electrons to the substrate (basal planes are oriented perpendicular to the substrate [83]), making them a very attractive morphology for hematite. This thermal oxidation method has been demonstrated on multiple (even transparent) substrates [84], and methods for doping the particles have been employed [78]. However, no realistic reports of activity toward water oxidation have appeared. This may be due to the defects present in nanowires prepared this way or the presence of suboxides near the interface of the substrate which greatly enhance recombination [85].

4.3.4 Electrochemical Fe_2O_3 Nanostructuring

The development of nanostructuring techniques using potentiostatic anodization has provided another possible route to create structured hematite photoelectrodes. While it has long been known that the potentiostatic anodization of certain metals can create structuring on small length scales, only recently have methods been developed to prepare ordered arrays of nanosized tubes or pillars with this technique. For example, ordered nanotube arrays of TiO_2 created using potentiostatic anodization have been successfully employed in multiple device applications including the solar photolysis of water [86]. Like the nanowire approach, these nanotube arrays have the potential to reduce crystal grain boundaries and enhance electron conduction to the current collector. In addition, the small thickness of the tube walls should allow for efficient hole collection. Recently, Grimes and coworkers showed that iron foils could be nanostructured using anodization in a glycerol-based electrolyte containing 1% NH_4F + 1% HF + 0.2% HNO_3 [87]. Ordered nanopores

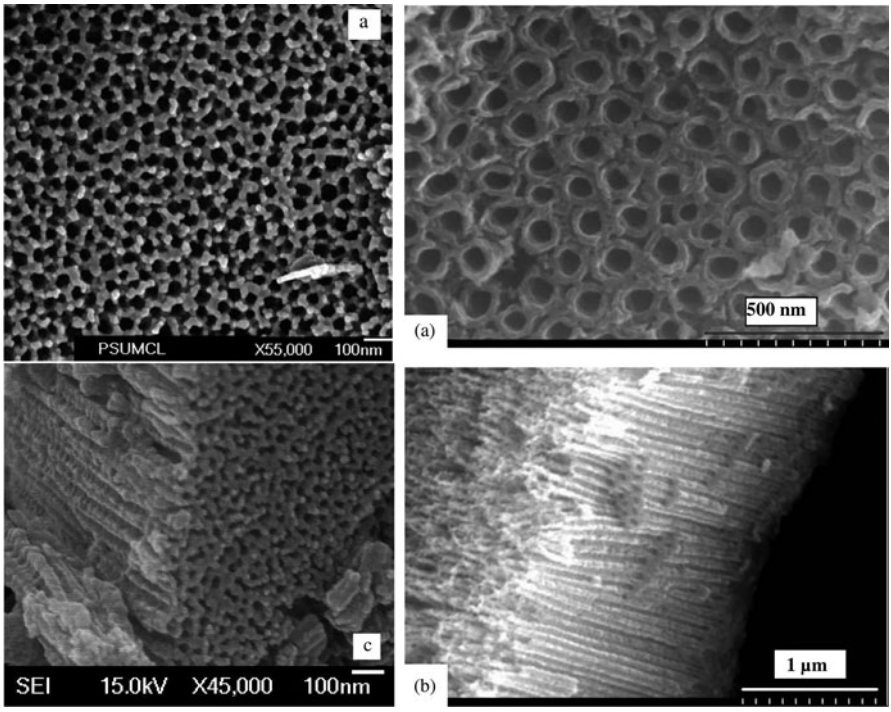

Fig. 4.6 Hematite morphologies accessible by potentiostatic anodization: The *left* (*top* and *bottom*) shows SEM images of structures from the work of Prakasam et al. [87] and the *right* (*top* and *bottom*) shows images of tubes from Rangaraju et al. [88]. SEM images used with permission from [87] and [88]

were observed with pore size ranging from 20 to 250 nm and depths up to 600 nm depending on the anodization voltage and time (see Fig. 4.6, left). Under simulated solar illumination these photoanodes produced a photocurrent of 0.05 mA/cm^2 at 0.4 V vs. SCE in 1 M NaOH. This current increased tenfold with the addition of 0.5 M H_2O_2 indicating good electron transport in these films, and suggesting the surface kinetics of the water oxidation reaction were limiting the water-splitting photocurrent. The same research group improved on this result by alloying the iron with titanium before anodization [89]. Water-splitting photocurrents were obtained from films that were 6.6% Fe, based on metal, and were largely anatase TiO_2. They observed reasonable photoactivity with a quantum efficiency of ca. 4% with 400 nm light at 1.5 V vs. RHE. In contrast to this Fe–Ti–O work, very well-defined nanotube arrays (see Fig. 4.6, right) created from pure iron foils have been subsequently reported by a different research group [88]. In this work, a single anodization step with 0.1 M NH_4F + 3 vol% water in ethylene glycol created nanotubes with walls less than 50 nm and lengths of about 1.5 µm. After an optimized annealing treatment these electrodes were found to be a mixture of both hematite and maghemite by XRD and had only small photocurrents (160 µA/cm^2, 1.23 V vs.

RHE in AM 1.5 light compared to 120 μA/cm^2 dark current). However, a double step anodization procedure with the addition of sodium tripolyphosphate in the electrolyte, and the subsequent annealing created a dendrite-like morphology situated over the tube array. Electrodes prepared this way exhibited a photocurrent of about 1 mA/cm^2 at AM 1.5 and 1.23 V vs. RHE. This is quite remarkable given the presence of maghemite and as the films were not intentionally doped to increase the carrier concentration. However, a large carrier concentration (10^{21} cm^{-3}) was found via Mott–Schottky indicating a large amount of dopant or impurity present. The authors attribute the high photocurrent to the double-layered structure which includes both a large surface area for water oxidation and a vertically orientated nanotube array for electron transport.

In subsequent work by the same group, a sono-electrochemical anodization method was employed to obtain either nanoporous or nanotubular Fe_2O_3 depending on the anodization conditions [90]. The optimization of conditions gave nanotubes with walls an impressive 5–6-nm thick and microns in length. Annealing these films resulted in pure hematite which gave similar photocurrents (ca. 1 mA/cm^2 at AM 1.5 and 1.23 V vs. RHE) and similar carrier densities to the previous work. While the initial tube size presented in this work is remarkable and an important step for obtaining hematite with the ideal morphology, the tubes were initially amorphous Fe_2O_3. The annealing step necessary for crystallinity and photoactivity probably demolishes the meticulous nanostructuring through a sintering process like has been observed for fine-structured hematite at high temperatures [67].

In addition to the nanostructuring of Fe_2O_3 with potentiostatic anodization, hematite photoanodes have been prepared by electrodepostion of precursors from solution. Recently, McFarland and coworkers reported an electrodeposition method of iron hydroxides from $FeCl_3$ solutions. The subsequent annealing at high temperature (700°C) then resulted in porous hematite films [20, 91]. This method readily allows for the incorporation of dopants which were found to have an effect on the morphology of the sintered electrodes. With feature sizes of 30–40 nm the observed IPCEs of 8% at 400 nm at 1.2 V vs. RHE in 1 M NaOH with 15% Mo doping are a notable result. However, the large particle size remains a limitation to higher photocurrents. Another example of electrodeposition has been recently reported by Spray and Choi [92] using an anodic method as opposed to the cathodic method investigated by the McFarland group. They were able to demonstrate impressive morphology control ranging from wire arrays to porous films by varying the solution pH. The films were photoactive in an electrolyte-containing iodide, but water oxidation photocurrents were not reported.

In general, it is clear that major advances have been made recently in the nanostructuring of hematite by electrochemical methods. However, the potential to oxidize water with hematite prepared in the methods described above has been limited by the crystallinity and ultimate feature size after the requisite annealing.

4.3.5 Spray Pyrolysis Techniques

The colloidal, nanowire, and anodization approaches to deliberately nanostructure hematite have provided great leaps in hematite nanostructuring but only moderate success so far for water-splitting photocurrents. However, from its first report [93] the spray pyrolysis (SP) method has continuously produced thin films of photoactive hematite. Typically, an aqueous or ethanolic solution of Fe^{3+} is simply sprayed onto a hot (~400°C) substrate and photocurrents in the 0.5–1.0 mA/cm^2 range can be obtained under simulated solar illumination (1 M NaOH, 1.6 V vs. RHE) [94–97] with the exception of one report [98] that is improbable in view of the action spectrum reported by the authors [99]. Surprisingly, modest photocurrents are obtained with this method even without intentionally adding dopants to increase the conductivity of the Fe_2O_3. However, it is likely that the commonly used precursors like $FeCl_3$ or $Fe(AcAc)_3$ leave chlorine or carbon residues behind that could act as electron donors. Typically, this technique can produce films with nanometer crystalline domain size, but the films are generally compact (not porous) and the surface area limits the conversion efficiency. However, the ease and reproducibility of the technique allow for fundamental studies on dopants [95, 100] and substrate effects [96], and careful optimization has produced films with a notable quantum efficiency (IPCE = 25% at 400 nm and 1.42 V vs. RHE) [100]. In a recent report from Duret and Grätzel, the spray pyrolysis technique was modified to create nanostructured films [94]. Here an ultrasonic spray nozzle was used to create very fine droplets of the precursor which were entrained in a flow of dry air and carried rapidly and horizontally over a heated substrate. The low concentration of the precursor in the gas stream allowed the slow growth (~100 nm/h) of mesoscopic hematite with a leaflet-type structure consisting of 100-nm-sized platelets with thickness of 5–10 nm bundled into 50 nm sheets oriented perpendicular to the F-doped SnO_2 support (see Fig. 4.7, top). These ultrasonic spray pyrolysis (USP) films were found to perform impressively for water splitting, producing 1.3 mA/cm^2 under AM 1.5 (100 mW/cm^2) simulated solar irradiation in 1 M NaOH with an applied potential of 1.23 V vs. RHE. The IPCE was found to be 16% with 375 nm illumination at the same applied potential, and over 30% at 1.6 V vs. RHE. This was a threefold increase over control films created by a conventional spray pyrolysis method in the same work, and even an improvement over optimized photoanodes created by SP [100]. The advantage of the nanostructured morphology could be directly observed by comparing normalized IPCEs of the UPS and SP electrodes (Fig. 4.7, bottom). The IPCE is higher for longer wavelengths (400–600 nm), indicating the more efficient conversion of holes due to the morphology. Subsequent work on these films revealed the importance of Si doping, and showed an enhanced (110) reflection from XRD as compared to powder samples indicating a preferred orientation of the (001) basal plane normal to the substrate [101, 102]. The vertical orientation of the (001) planes is thought to be very important to the conduction of photogenerated electrons to the conducting substrates, as this is the least resistive direction of conduction in hematite.

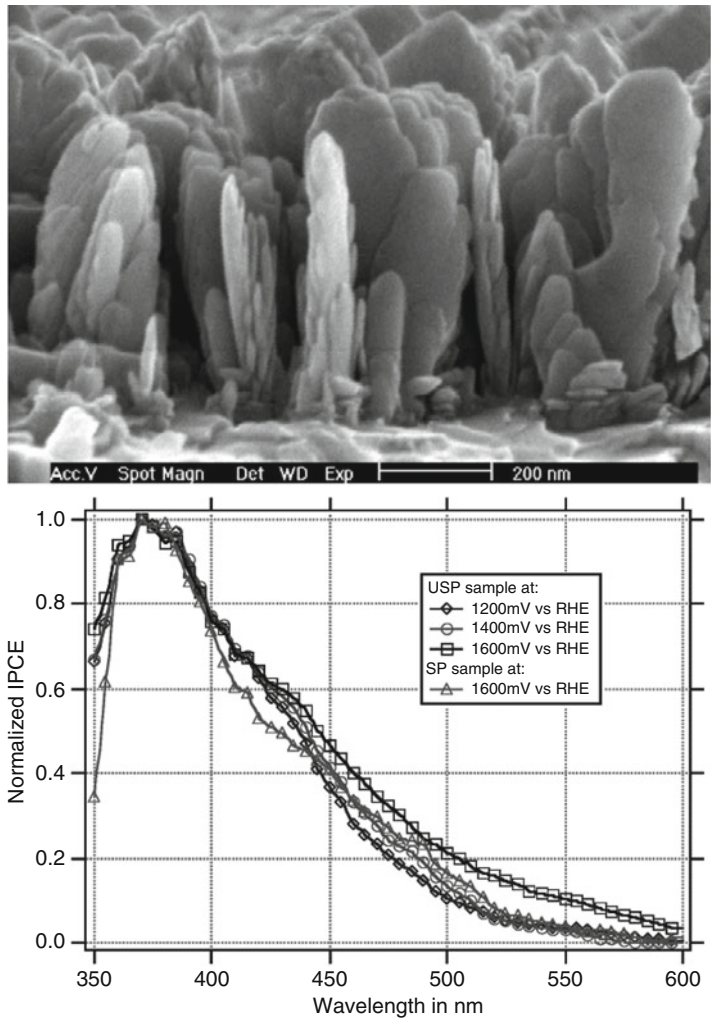

Fig. 4.7 Hematite films created by USP show a platelet morphology by cross-sectional SEM analysis (*top*, from [101]), and an increased IPCE at longer wavelengths compared to films created by conventional spray pyrolysis (*bottom*, from [94], used with permission)

However, because the larger surface of the platelets is the basal plane, this morphology also requires the holes to be conducted across oxygen layers. This detail and the poor kinetics of water oxidation were thought to be limiting the performance in this system.

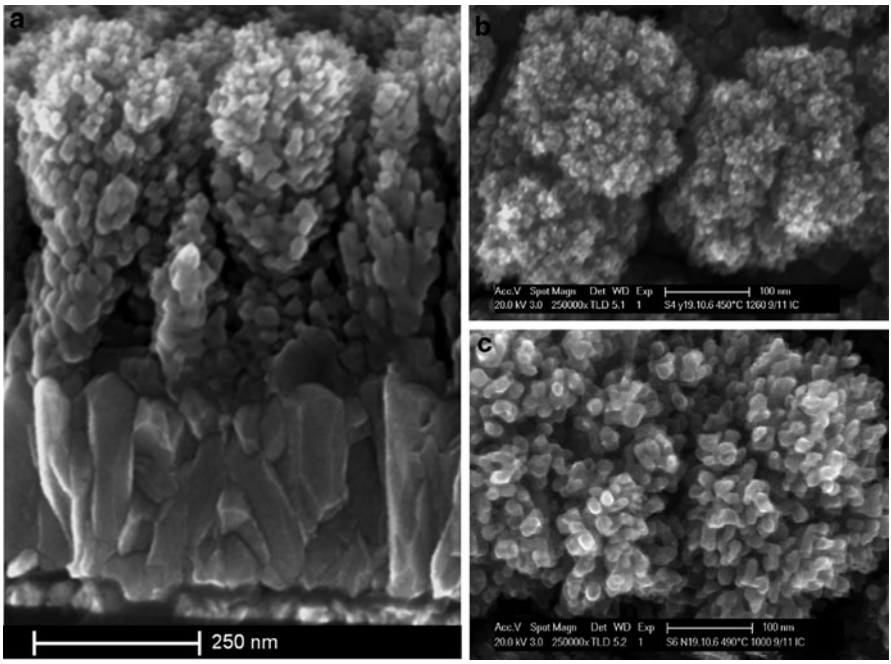

Fig. 4.8 Morphology of Si-doped hematite films created by the APCVD technique as observed by SEM. The left side shows a cross-sectional view of the Fe_2O_3, prepared at a substrate temperature of 420°C (heater setpoint of 470°C), on top of the F:SnO_2 substrate. The right shows top-down views of films prepared with heater set points of 450°C (*above*) and 490°C (*below*). From [13] used with permission

4.3.6 Atmospheric Pressure Metal Organic CVD

Continuing efforts from Grätzel and coworkers to perfect the nanometer length scale morphology of hematite thin films for water splitting beyond the USP films have led to the development of a simple, yet effective process to make nanostructured films of hematite found to be highly active for water photooxidation (Fig. 4.8). This method is based on the thermal decomposition of iron pentacarbonyl in an atmospheric pressure chemical vapor deposition (APCVD) reactor. $Fe(CO)_5$ vapors are transported, along with tetraethyl orthosilicate (TEOS) as a source of silicon dopant, by an air stream vertically to a substrate maintained at 420°C. This high temperature and the poor thermal stability of the $Fe(CO)_5$ (the half-life for decomposition at 300°C is 5.3 ms [103]) causes the homogenous nucleation of nanoparticles in the gas phase [104]. These particles are then subjected to a thermophoretic force which limits their approach to the hot substrate and results in fractal-like cauliflower structures suggesting a diffusion-limited aggregation (rather than surface reaction limited) mechanism [13]. Similar to the films prepared by the USP method, the silicon dopant was found to affect the

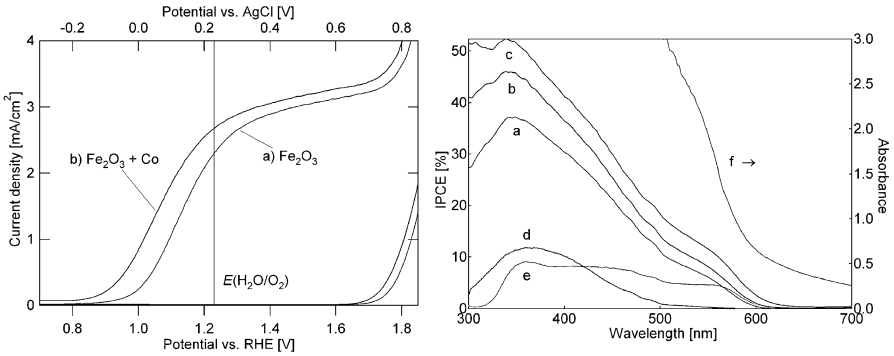

Fig. 4.9 Photoelectrochemical characterization of Si-doped Fe_2O_3 electrodes prepared by the APCVD technique. The *left graph* shows the current-voltage characteristics in darkness and under simulated sunlight (100 mW/cm^2) at a scan rate of 50 mV/s. (**a**) Unmodified Fe_2O_3; (**b**) the same electrode after cobalt treatment. The right graph shows the incident photon-to-current efficiency (IPCE) spectrum of the same electrode at different conditions. (**a**) Unmodified Fe_2O_3 at 1.23 V_{RHE}; (**b**) after cobalt deposition, at 1.23 V_{RHE}, (**c**) at 1.43 V_{RHE}, (**d**) at 1.03 V_{RHE}, (**e**) at 1.23 V_{RHE} but illuminated through the SnO_2 substrate; (**f**) absorption spectrum of this electrode. From [105] used with permission

nanostructure, producing a smaller feature size in both cases and an alignment of the basal crystal plane normal to the substrate [102, 105]. While this latter observation is considered to be a major factor improving the performance of these electrodes by facilitating electron transport to the collector, another report found the crystalline orientation of hematite unimportant to the performance [106].

The optimization of the APCVD deposition technique led to films producing a photocurrent of 1.8 mA/cm^2 at 1.23 V vs. RHE under simulated solar illumination (AM 1.5, 100 mW/cm^2) in 1 M NaOH. This was further increased to 2.2 mA/cm^2 by treating the surface with Co^{2+} ions, which act to lower the energy barrier for water oxidation and reduce the applied potential needed [105] (see also Sect. 4.4.2). With IPCEs of 42% at $\lambda = 370$ nm and 1.23 V vs. RHE these electrodes represent the most efficient Fe_2O_3 photoanodes for water oxidation to date –surpassing even the single-wavelength quantum efficiencies of Nb-doped α-Fe_2O_3 single crystals (IPCE = 37% at 370 nm and 1.23 V vs. RHE) [53]. This benchmark performance corresponds to 3.3% STH conversion efficiency when used in a tandem configuration (see Sect. 4.4.1). The PEC characterization of this champion electrode is shown in Fig. 4.9. Particularly notable is the increased IPCE of the photoanodes at wavelengths between 500 and 600 nm as compared to the Fe_2O_3 film prepared by the USP method [94] and especially the single crystal electrodes shown in Fig. 4.3. Because the high surface area and small feature size of the APCVD films the photocurrent action spectrum is much broader than the single crystal results: photons with longer wavelength have a higher chance for being absorbed within the hole diffusion length, resulting in much higher solar photocurrents than the single crystal electrodes.

In continuing work with this deposition technique Cesar et al. [13] examined the deposition mechanism, and showed a large temperature effect on the nanostructure which corresponded to the performance of the electrodes. In addition, the electrodes were studied by impedance spectroscopy; a Mott–Schottky analysis gave the calculated donor density of the Si-doped Fe_2O_3 films as 1.7×10^{20} cm^{-3} – close to the predicted 6×10^{20} cm^{-3} if all of the 1.6 at% Si [105] was substitutionally incorporated into the lattice as Si^{4+}. This observation suggests that a space charge layer of ~5 nm could be present and aiding hole transport the SCLJ even in the small features on the top of the APCVD film. The high donor density also created good electron conductivity and films up to 1 μm delivered similar photocurrents as thinner films when illuminated from the semiconductor/electrolyte interface even though photons were absorbed further from the conducting substrates. This suggests that electron percolation through the film is not a limiting factor.

Recently another group has reported the application of the APCVD technique for Fe_2O_3 photoanodes using both ferrocene and iron pentacarbonyl as iron sources, and different sources of Si for doping [107, 108]. First, ferrocene as a precursor was shown to be effective in preparing photoactive Fe_2O_3 films without a separate dopant species [108]. Photocurrents were ca. 0.6 mA/cm^2 at 1.23 V vs. RHE in 1 M NaOH under simulated solar irradiation. Furthermore, the larger feature size observed in the ferrocene-prepared electrodes (50–100 nm) as compared to the $Fe(CO)_5$ indicates the importance of the decomposition of the carbonyl precursor and the nucleation of nanoparticles before reaching the hot substrate. Next, the silicon doping was studied by varying the Si precursor species and feed rate [107]. In addition to TEOS, tetramethyl orthosilicate (TMOS) was also found to be an effective source of Si. XPS studies verified the +4 oxidation state of Si in both cases. In addition, trimethyl orthoformate (TMOF) was used as a silicon-free control, and resulted in electrodes with significantly less photocurrent. Although their findings did not result in a definitive explanation of the silicon's role, it did suggest that a combination of factors including the formation of lattice defects and nanoparticle cluster formation caused by the Si precursor's decomposition and incorporation, additional to the classical doping effect, may be contributing to the high performance observed in these electrodes.

Despite the impressive performance of the APCVD iron oxide films the solar photo current remains low compared to the theoretical value of 12.6 mA/cm^2 predicted for a material with this bandgap [6]. This is because, despite absorbing almost all of the light (see Fig. 4.9, left, curve f) the quantum conversion efficiencies are relatively low and are especially poor (<20%) in the region where hematite has an indirect bandgap transition (λ = 610–450 nm). Importantly, there is over 10 mA/cm^2 of solar photocurrent available in this wavelength range. The poor performance can be primarily attributed to the cauliflower-type morphology. While this morphology has an appropriate feature size of 10 nm at the SCLJ, the individual cauliflower structures consist of thick stems which increase the number of photons absorbed far from the SCLJ.

4.3.7 *Extremely Thin Absorber–Host-Scaffold Approach*

In an extension of the stacked thin film approach proposed by Itoh and Bockris [55] an increased photoresponse should also be obtainable with hematite by coating a thin film conformally on a suitable nanostructured collector with a large specific surface area, in analogy to the dye-sensitized solar cell (DSC) [109] and similar extremely thin absorber (ETA) photovoltaics [110]. In the case of the DSC, the photoanode is constructed from a light-absorbing dye molecule anchored to a high surface area mesoporous TiO_2 scaffold, which collects and transports the photoexcited electrons. The DSC's host-scaffold/guest-absorber approach effectively decouples light harvesting and charge transport while maximizing the IPCE by means of the thin (mono)layer of absorber on the high surface area, transparent collector. Given the success of this concept for photovoltaic energy conversion as well as the light absorbing and photogenerated hole transport limitations of α-Fe_2O_3, this is a promising direction for increasing the quantum efficiency of hematite.

A difficulty in applying this method for hematite is finding a suitable host material which satisfies the following criteria: First, the conduction band of the scaffold material must lie lower in energy than the conduction band of hematite to allow efficient electron transport across the host/guest interface and second, the scaffold material should have a larger band gap than hematite so as to not compete with the light absorption. Few oxide semiconductors meet both of these requirements. However, Grätzel and coworkers have recently demonstrated this concept for hematite photoanodes using nanostructured WO_3 as the host scaffold [8]. In this work the host scaffold was coated with a thin layer (ca. 60 nm) of Fe_2O_3 by the APCVD method (see Fig. 4.10, top) and a 20% increase in the photocurrent was observed over control samples prepared on the flat F:SnO_2 substrates. This increase was attributed to an increase in the absorbed photon-to-current efficiency (APCE), especially in the wavelength range from 500–600 nm (Fig. 4.10, bottom).

While this demonstration of the host/guest approach indicates it is a promising and accessible methodology to fully exploit the light harvesting capabilities of hematite for solar water splitting, the best results were obtained with iron oxide coatings 60 nm thick over the host scaffold. This is too thick based on the hole transport limitations already discussed. Attempts to use thinner films of iron oxide resulted in poor performance, similar to other reports of thin films Fe_2O_3 [54]. Further understanding and control of the interface between the iron oxide and the conducting substrate as well as the electronic properties and crystallinity of ultrathin films of Fe_2O_3 are necessary to advance this promising nanostructuring approach.

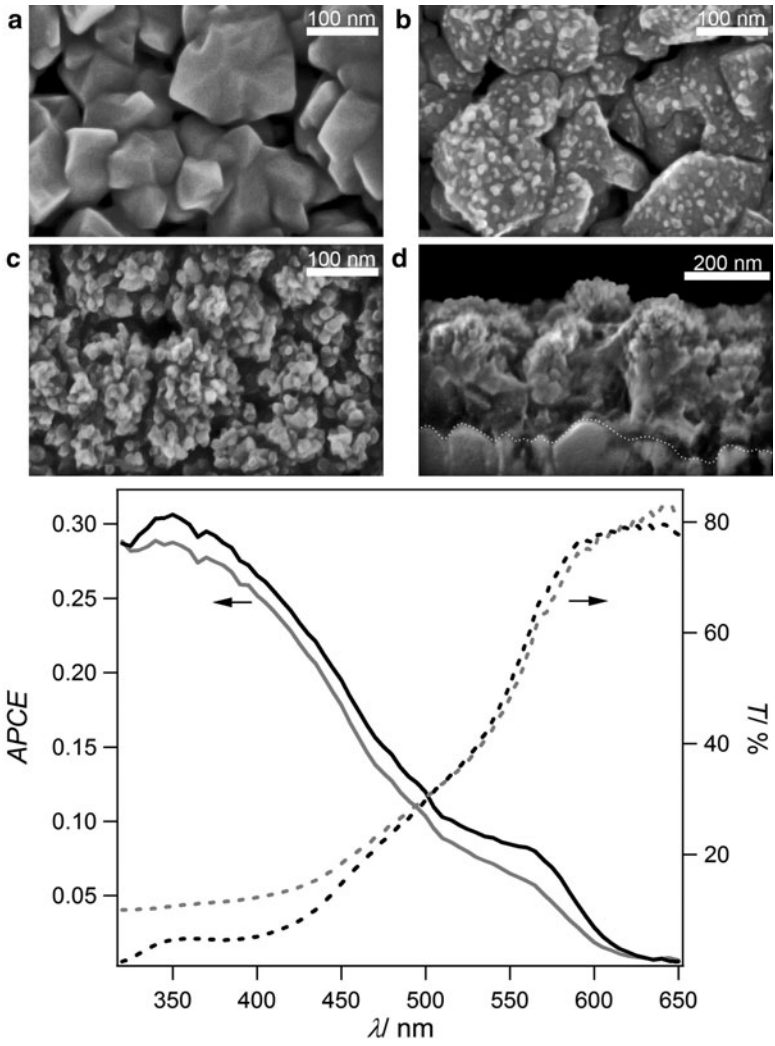

Fig. 4.10 (*Top*) Scanning electron micrographs of the WO_3/Fe_2O_3 host/guest system. Image (**a**) shows the morphology of the WO_3 host scaffold before iron oxide deposition. After 1 min of Fe_2O_3 deposition at the standard deposition rate (~100 nm/min) the WO_3 film is covered in iron oxide nanoparticles (**c**) while at a lower deposition rate (~10 /min, edge of growth spot) the iron oxide nanoparticles are seen just starting to cover the WO_3 scaffold (b). The cross-section of the film, corresponding to (**c**), is shown in (**d**). (*Bottom*) The APCE (*solid lines*) at 1.43 V_{RHE} and the transmittance, *T* (*broken lines*) of photoanodes prepared with a 1-min Fe_2O_3 deposition time plotted against the incident light wavelength, λ. The host/guest and the control electrode responses are indicated by *dark* and *light lines*, respectively

Table 4.1 Comparison of hematite photoanode structuring methods

Technique	Feature size	Dopant	Performance	References
Single crystal	Micron	Nb	IPCE 37% at 370 nm and 1.2 V_{RHE}	[53]
Sintered polycrystalline disk	Micron	Si	IPCE 34% at 400 nm and 1.23 V_{RHE}	[45]
Colloidal deposition of porous films	50 nm	None	IPCE 1% at 400 nm and 1.4 V_{RHE}	[67]
Solution-based nanowires	50 nm × 500 nm	None	IPCE 7% at 400 nm and 0.9 V_{RHE} (in KI)	[19]
Potentiostatic anodization (nanotubes)	6 nm × 1 μm	None	Before annealing: none reported After annealing[a]: 1.0 mA/cm^2 at 1.23 V_{RHE} and AM 1.5 (87 mW/cm^2)	[90]
Electrodeposition	20 − 50 nm	Mo	IPCE 8% at 400 nm and 1.2 V_{RHE}	[20]
Ultrasonic spray pyrolysis	10 nm × 300 nm	Si	1.5 mA/cm^2 at 1.23 V_{RHE} and AM 1.5 (100 mW/cm^2) and IPCE 14% at 400 nm and 1.23 V_{RHE}	[94, 101]
Atmospheric pressure CVD	5 nm × 300 nm	Si	2.2 mA/cm^2 at 1.23 V_{RHE} and AM 1.5 (100 mW/cm^2) and IPCE 36% at 400 nm (42% at 370 nm) and 1.23 V_{RHE}	[105]
Extremely thin absorber	50 nm film	Si	1.3 mA/cm^2 at 1.23 V_{RHE} and AM 1.5 (100 mW/cm^2) and IPCE 26% at 400 nm and 1.43 V_{RHE}	[8]

[a]Feature size not reported after annealing

4.3.8 Nanostructuring Method Comparison

Many different approaches have been taken to nanostructure Fe_2O_3 for use in PEC water splitting, and at least as many methods of characterizing the electrodes have also appeared. As such it can be difficult to compare the results in the literature, especially when variations in light sources give large over-estimations of photocurrents due to superfluous UV light. A recent and important contribution by Murphy et al. addresses these issues and suggests reliable methods for evaluating electrode conversion efficiencies [6]. While not all of the reports discussed in this section have followed these suggestions it can still be helpful to compare the top performances from the different structuring techniques and the resulting performance. This is done in Table 4.1.

It is clear, by looking at Table 4.1, that while many methods of structuring hematite have been reported, the IPCE values at ca. 400 nm rarely come close that of the single crystal or sintered polycrystalline electrodes prepared during the first

decade of work. Even the champion electrodes made by APCVD merely match the IPCE of the single crystal work at ca. 400 nm without the enhanced surface treatment. The key to the increased photocurrents in the APCVD electrodes has, of course, been the nanostructuring, which allows for the more efficient conversion of the longer wavelengths of light. Further work on the nanostructuring will, no doubt, see solar photocurrents rise, but the increase in IPCE beyond 40% at 400 nm and 1.23 V_{RHE} will require research to tackle hematite's other remaining challenges.

4.4 Overcoming Hematite's Remaining Challenges

Many techniques have been used to nanostructure hematite, and while clear advances have been made over planar, single crystal approaches, in general the performance of nanostructured electrodes has remained poor compared to the quantum efficiencies found in optimized photoanodes prepared from TiO_2 or WO_3. While this is partly due to the absence of a method to prepare a "perfect" nanostructure, there are still limitations in (1) the understanding of the critical material properties affecting efficiencies and (2) the surface oxidation reaction kinetics. In addition, based on the flatband potential of hematite it cannot be used to split water unassisted by a bias voltage. In this section, these limitations are clearly detailed and new promising approaches to overcome these remaining challenges are reviewed.

4.4.1 Flatband Potential and Tandem Cell Approach

As mentioned in Sect. 4.2.5, one of the major drawbacks of hematite is that its flat band potential is below the water reduction potential. This means that the electrons exiting the conduction band of hematite and traveling to the cathode do not have sufficient energy to reduce water and create hydrogen; a small external bias must be added to hematite to complete the water-splitting reaction. The overall efficiency of solar water splitting then must account for the power input by this external bias. However, a clever solution to this problem was invented by Augusttynski and Grätzel [111]. Since hematite only absorbs solar irradiation up to wavelengths of 600 nm, transmitted photons ($\lambda > 600$ nm) can be converted by another photosystem to provide the necessary potential to complete the water-splitting reaction and accomplish unassisted solar hydrogen production from water. This second photosystem is most practically a photovoltaic device as photocathode materials typically suffer from stability issues. A promising candidate for this photovoltaic device is the DSC as these devices can be produced for one-third to one-fifth the cost of a conventional silicon solar cell and the absorption range can be tuned by selecting the appropriate dye.

Ideally in this hematite/DSC water-splitting tandem cell, only one photovoltaic system would provide the necessary potential to complete the water-splitting reaction. However, due to the large overpotential needed for water oxidation (see Sect. 4.4.2) and other loss processes, two solar cells are needed to provide enough voltage to the current state-of-the-art Fe_2O_3. For example, saturation (plateau) photocurrents from Fe_2O_3 prepared from APCVD are not reached until 1.4 V vs. RHE. While a traditional solution can still be envisioned with two solar cells with half the active area each behind the hematite photoanode, the recent development of new dyes for the DSC opens up new possibilities for optimizing light harvesting in these water-splitting tandem cells. Different architectures for the hematite/DSC system were recently investigated by Brillet et al. [112] and it was found that a three-level tandem (hematite/suqarane dye DSC/black dye DSC) was the most efficient at splitting water with a calculated overall efficiency of 1.4% solar to hydrogen. This is much lower than the predicted 3.3% with this system based on iron oxide photocurrent alone, and losses were attributed to light scattering and the large overpotential for water oxidation by hematite.

A tandem cell configuration would not be needed if the flat band potential of hematite could be shifted so that water could be directly split by solar light. While numerous groups have reported a V_{fb} 0.3 − 0.4 V lower than the hydrogen evolution potential [14], Hu et al. recently suggested that a CoF_3 treatment of Ti-doped Fe_2O_3 could actually shift the flat band potential and allow the direct hydrogen production by hematite [113]. While additional investigation of this claim is necessary to verify sustained hydrogen production at zero bias, it is indeed a promising route to reduce or eliminate the necessary applied bias.

4.4.2 Oxygen Evolution Overpotential and Surface Catalysis

Based on the flat band potential of hematite an external bias of only 0.3–0.4 V vs. RHE should be necessary to initiate the water-splitting reaction. Once the applied bias is greater than the flatband potential, the band bending will drive photogenerated holes to the surface for reaction. However, photocurrent onset potentials are usually not observed until 0.8–1.0 V vs. RHE even for the single crystal electrodes. The remaining potential of ca. 0.5 V is due to the overpotential for water splitting caused by unfavorable surface properties. These unfavorable properties have two origins. First, there is evidence that oxygen vacancies [17, 23, 46] and crystalline disorder [13] can be present at the surface. This would create additional Fe^{2+} recombination centers for holes, and can even result in Fermi level pinning in some electrodes [94]. Second, the reaction kinetics for water oxidation are slow, not just due to the complicated four-electron mechanism that must occur, but also compared to other oxide semiconductors [79]. This may be due to the more pronounced metal 3d character of the valence band compared to other oxides [23].

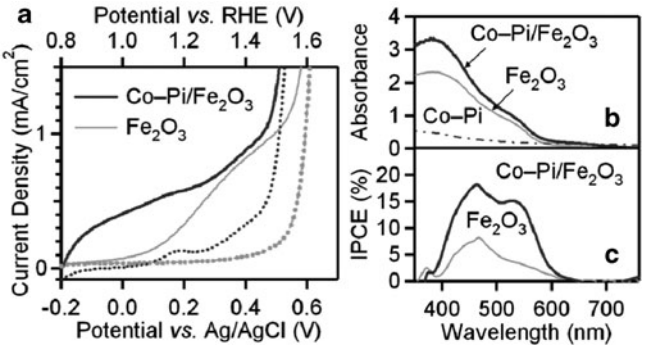

Fig. 4.11 Water splitting with hematite and a cobalt-phosphate-based catalyst: (**a**) Dark (*dashed*) and photocurrent (*solid*) densities for α-Fe_2O_3 (*light*) and Co-Pi/α-Fe_2O_3 (*dark*) photoanodes, collected using simulated AM 1.5 illumination (1 sun, backside illumination) at a scan rate of 50 mV/s. (**b**) Electronic absorption and (**c**) IPCE spectra for α-Fe_2O_3 and Co-Pi/ α-Fe_2O_3 (at 1.23 and 1 V vs. RHE, respectively). The absorption spectrum of Co-Pi on FTO without α-Fe_2O_3 is included in (**b**), but no photocurrent was detected for these anodes. From [116] used with permission

The first surface challenge can be addressed by strong oxidation conditions [46] and careful hematite preparation, but the slow water oxidation kinetics are probably intrinsic to hematite. Nevertheless, methods have recently been found to increase the oxidation rate and thus reduce the overpotential. For example, the water oxidation by cobalt has been extensively studied and is known to be particularly rapid [114]. Indeed the treatment of Fe_2O_3 photoanodes (prepared by APCVD) with a monolayer of Co^{2+} resulted in a ca. 0.1 V reduction of the photocurrent onset potential [105]. Since this treatment also increased the plateau photocurrent it is good evidence that the reaction rate was increased, and the Co^{2+} did not just fill surface traps. Following the report of a remarkably effective cobalt-phosphate (Co-Pi)- based water oxidation catalyst [115], the overpotential was reduced even further on hematite photoanodes by Gamelin and coworkers [116]. Their results are shown in Fig. 4.11.

The application of the Co-Pi catalyst resulting in a shift of the onset potential by 0.25 V. The effect is further supported by the increase in IPCE seen in Fig. 4.11. Applying this treatment to the high performance Fe_2O_3 anodes could possibly result in photocurrents nearing 3 mA/cm^2 at 1.23 V vs. RHE. Further work is necessary to understand the effect of this catalyst over the standard Co^{2+} treatment, and to better characterize the reaction mechanism occurring at the surface of both treated and untreated hematite. Interestingly, recent reports describe a very complex anisotropic reactivity of hematite at the SCLJ due to the anisotropic crystal structure and exposed crystalline planes [117, 118]. Fully exploiting the most reactive crystal face of hematite might further reduce the required overpotential for water oxidation.

4.4.3 Continued Material Considerations

To conclude, it is clear there is a strong dependence of the performance of synthetic hematite on the deposition technique. While methods such as spray pyrolysis and CVD consistently produce electrodes photoactive for water oxidation, solution-based methods such as sol–gel approaches have failed to produce especially photoactive hematite. This is certainly related to the quality of the prepared material in terms of crystallinity and impurity concentrations. Aqueous methods of preparing hematite typically pass through a phase containing iron hydroxide (e.g., akaganeite, lepidocrocite, or goethite) but primarily hematite is detected after at annealing at 500°C. However, it has been shown that at temperatures up to 800°C, a nonstoichiometric composition remains in hematite when prepared in this way [119]. This results in a distortion in the crystal structure due to cation vacancies and remaining hydroxides. A structural temperature dependence has also been shown to affect the color of hematite due to the subtle relaxation of the iron positions in the crystal lattice and the resulting change in the optical reflectivity [120]. This was observed to occur at similar temperatures of 800°C. In addition, nanoparticles of hematite prepared via an aqueous precipitation have shown a size and temperature-dependent concentration of spinel defects at the surface. The formation of these defects on hematite was shown to be governed by the thermodynamics of the α–γ phase transition with decreasing particle size [121]. Raman spectroscopy has shown that similar defects on the surface of highly efficient anodes prepared by APCVD are important to the performance [13].

The above factors can all play a major role in both surface and bulk recombination, and thus care must be taken to prepare and characterize hematite for PEC application. Empirically, these problems can be avoided by simply heating the electrode to sufficiently high temperatures as was done with the sintered polycrystalline work [28] or the recent work by McFarland and coworkers [20, 91]. However, there is a clear tradeoff between phase purity and feature size as at high temperatures rapid sintering of nanostructures occurs. In general, the important material parameters needed to produce highly photoactive hematite must be clarified in order to be able to apply the most appropriate nanostructuring technique and obtain an ideal morphology while still ensuring photoactivity.

In addition to the structural properties, there is an unmistakable need to increase understanding of the hematite–substrate interface. A photoinactive “dead layer” has been observed in hematite near the surface of the supporting electrode [8, 13, 54, 105] which can be ameliorated with the addition of an ultra-thin Si-based insulating layer [105]. While fundamental studies of this “dead layer” have increased understanding and further reduced its effect [96], the ability to create ultra-thin films (~20 nm) of hematite with quantum efficiencies (APCEs) matching the single crystal or Si-doped APCVD electrodes has not yet been demonstrated. A fundamental understanding of hematite/conductor interfaces is needed to overcome this issue which currently limits its application to ETA configurations.

Finally, the low quantum efficiencies (even at short wavelengths in optimized single crystal photoanodes), the ultrafast carrier recombination, and the interbandgap states found in hematite suggest that this material possesses intrinsic limitations that will be difficult, if not impossible, to resolve given our lack of understanding. However, recent combinatorial efforts to optimize both the alloy composition [122, 123] and doping in hematite [124] suggest that some improvement can be made of the standard "single dopant" approach. For example, the proper doping with multiple atoms may increase the hole and electron mobilities by changing the dielectric constant of the crystalline phase. Continued efforts along these lines and further fundamental studies of the PEC properties of hematite are necessary, parallel with the nanostructuring efforts, to completely harness the potential of hematite for solar water splitting. Indeed, since the initial writing of this chapter many important advances already have been reported in the performance and understanding of hematite [125] and many more are sure to follow.

References

1. Fujishima, A., Honda, K.: Electrochemical photolysis of water at a semiconductor electrode. Nature **238**, 37 (1972)
2. Grätzel, M.: Photoelectrochemical cells. Nature **414**, 338 (2001)
3. Khaselev, O., Turner, J.A.: A monolithic photovoltaic-photoelectrochemical device for hydrogen production via water splitting. Science **280**, 425 (1998)
4. Ni, M., Leung, M.K.H., Leung, D.Y.C., Sumathy, K.: A review and recent developments in photocatalytic water-splitting using TiO_2 for hydrogen production. Renew. Sust. Energ. Rev. **11**, 401 (2007). doi:10.1016/j.rser.2005.01.009
5. Santato, C., Ulmann, M., Augustynski, J.: Photoelectrochemical properties of nanostructured tungsten trioxide films. J. Phys. Chem. B **105**, 936 (2001)
6. Murphy, A.B., Barnes, P.R.F., Randeniya, L.K., Plumb, I.C., Grey, I.E., Horne, M.D., Glasscock, J.A.: Efficiency of solar water splitting using semiconductor electrodes. Int. J. Hydrogen Energy **31**, 1999 (2006). doi:DOI 10.1016/j.ijhydene.2006.01.014
7. Cornell, R.M., Schwertmann, U.: The iron oxides: structure, properties, reactions, occurrences, and uses. Wiley-VCH, Weinheim (2003)
8. Sivula, K., Le Formal, F., Grätzel, M.: WO_3–Fe_2O_3 photoanodes for water splitting: a host scaffold. Guest absorber approach. Chem. Mater. **21**, 2862 (2009). doi:10.1021/cm900565a
9. Zboril, R., Mashlan, M., Petridis, D.: Iron(III) oxides from thermal processes-synthesis, structural and magnetic properties, Mossbauer spectroscopy characterization, and applications. Chem. Mater. **14**, 969 (2002). doi:10.1021/cm0111074
10. Iordanova, N., Dupuis, M., Rosso, K.M.: Charge transport in metal oxides: a theoretical study of hematite alpha-Fe_2O_3. J. Chem. Phys. **122**, 144305 (2005)
11. Wang, X.O., Gao, L.S., Zheng, H.G., Ji, M.R., Shen, T., Zhang, Z.: Fabrication and electrochemical properties of alpha-Fe_2O_3 nanoparticles. J. Cryst. Growth **269**, 489 (2004). doi:10.1016/j.jcrysgro.2004.05.081
12. Hermanek, M., Zboril, R., Medrik, N., Pechousek, J., Gregor, C.: Catalytic efficiency of iron (III) oxides in decomposition of hydrogen peroxide: competition between the surface area and crystallinity of nanoparticles. J. Am. Chem. Soc. **129**, 10929 (2007)
13. Cesar, I., Sivula, K., Kay, A., Zboril, R., Grätzel, M.: Influence of feature size, film thickness, and silicon doping on the performance of nanostructured hematite photoanodes for solar water splitting. J. Phys. Chem. C **113**, 772 (2009). doi:10.1021/jp809060p

14. Lindgren, T., Vayssieres, L., Wang, H., Lindquist, S.E.: Photo-oxidation of water at hematite electrodes. In: Kokorin, A.I., Bahnemann, D.W. (eds.) Chemical Physics of Nanostructured Semiconductors, pp. 83–103. VSP International Science Publishers, The Netherlands (2003)
15. Marusak, L.A., Messier, R., White, W.B.: Optical-absorption spectrum of hematite, alpha-Fe_2O_3 near IR to UV. J. Phys. Chem. Solids **41**, 981 (1980)
16. Galuza, A.I., Beznosov, A.B., Eremenko, V.V.: Optical absorption edge in alpha-Fe_2O_3: the exciton-magnon structure. Low Temp. Phys. **24**, 726 (1998)
17. Gardner, R.F.G., Tanner, D.W., Sweett, F.: Electrical properties of alpha ferric oxide. 2. Ferric oxide of high purity. J. Phys. Chem. Solids **24**, 1183 (1963)
18. Kennedy, J.H., Frese, K.W.: Photo-oxidation of water at Alpha-Fe_2O_3 electrodes. J. Electrochem. Soc. **125**, 709 (1978)
19. Beermann, N., Vayssieres, L., Lindquist, S.E., Hagfeldt, A.: Photoelectrochemical studies of oriented nanorod thin films of hematite. J. Electrochem. Soc. **147**, 2456 (2000)
20. Kleiman-Shwarsctein, A., Hu, Y.S., Forman, A.J., Stucky, G.D., McFarland, E.W.: Electrodeposition of alpha-Fe_2O_3 doped with Mo or Cr as photoanodes for photocatalytic water splitting. J. Phys. Chem. C **112**, 15900 (2008)
21. Debnath, N.C., Anderson, A.B.: Optical-spectra of ferrous and ferric oxides and the passive film - a molecular-orbital study. J. Electrochem. Soc. **129**, 2169 (1982)
22. Kennedy, J.H., Frese, K.W.: Flatband potentials and donor densities of polycrystalline alpha-Fe_2O_3 determined from Mott-Schottky plots. J. Electrochem. Soc. **125**, 723 (1978)
23. Dareedwards, M.P., Goodenough, J.B., Hamnett, A., Trevellick, P.R.: Electrochemistry and photoelectrochemistry of iron(III) oxide. J. Chem. Soc. Faraday Trans. **79**, 2027 (1983)
24. Catti, M., Valerio, G., Dovesi, R.: Theoretical-study of electronic, magnetic, and structural-properties of alpha-Fe_2O_3 (hematite). Phys. Rev. B **51**, 7441 (1995)
25. Velev, J., Bandyopadhyay, A., Butler, W.H., Sarker, S.: Electronic and magnetic structure of transition-metal-doped alpha-hematite. Phys. Rev. B **71**, 205208 (2005)
26. Butler, W.H., Bandyopadhyay, A., Srinivasan, R.: Electronic and magnetic structure of a 1000 K magnetic semiconductor: alpha-hematite (Ti). J. Appl. Phys. **93**, 7882 (2003)
27. Ma, Y., Johnson, P.D., Wassdahl, N., Guo, J., Skytt, P., Nordgren, J., Kevan, S.D., Rubensson, J.E., Böske, T., Eberhardt, W.: Electronic structures of alpha-Fe_2O_3 and Fe_3O_4 from O K-edge absorption and emission spectroscopy. Phys. Rev. B **48**, 2109 (1993)
28. Kennedy, J.H., Anderman, M., Shinar, R.: Photoactivity of polycrystalline alpha-Fe_2O_3 electrodes doped with group IVa elements. J. Electrochem. Soc. **128**, 2371 (1981)
29. McGregor, K.G., Calvin, M., Otvos, J.W.: Photoeffects in Fe_2O_3 sintered semiconductors. J. Appl. Phys. **50**, 369 (1979)
30. Turner, J.E., Hendewerk, M., Parmeter, J., Neiman, D., Somorjai, G.A.: The characterization of doped iron-oxide electrodes for the photodissociation of water – stability, optical, and electronic-properties. J. Electrochem. Soc. **131**, 1777 (1984)
31. Launay, J.C., Horowitz, G.: Crystal-growth and photo-electrochemical study of Zr-doped alpha-Fe_2O_3 single-crystal. J. Cryst. Growth **57**, 118 (1982)
32. Cherepy, N.J., Liston, D.B., Lovejoy, J.A., Deng, H.M., Zhang, J.Z.: Ultrafast studies of photoexcited electron dynamics in gamma- and alpha-Fe_2O_3 semiconductor nanoparticles. J. Phys. Chem. B **102**, 770 (1998)
33. Joly, A.G., Williams, J.R., Chambers, S.A., Xiong, G., Hess, W.P., Laman, D.M.: Carrier dynamics in alpha-Fe_2O_3 (0001) thin films and single crystals probed by femtosecond transient absorption and reflectivity. J. Appl. Phys. **99**, 053521 (2006). doi:10.1063/1.2177426
34. Ahmed, S.M., Leduc, J., Haller, S.F.: Photoelectrochemical and impedance characteristics of specular hematite. 1. Photoelectrochemical, parallel conductance, and trap rate studies. J. Phys. Chem. **92**, 6655 (1988)
35. Horowitz, G.: Capacitance voltage measurements and flat-band potential determination on Zr-doped alpha-Fe_2O_3 single-crystal electrodes. J. Electroanal. Chem. **159**, 421 (1983)

36. Morin, F.J.: Electrical properties of alpha-Fe_2O_3 and alpha-Fe_2O_3 containing titanium. Phys. Rev. **83**, 1005 (1951)
37. Morin, F.J.: Electrical properties of alpha-Fe_2O_3. Phys. Rev. **93**, 1195 (1954)
38. Bosman, A.J., Vandaal, H.J.: Small-polaron versus band conduction in some transition-metal oxides. Adv. Phys. **19**, 1 (1970)
39. Chang, R.H., Wagner, J.B.: Direct-current conductivity and iron tracer diffusion in hematite at high-temperatures. J. Am. Ceram. Soc. **55**, 211 (1972)
40. Goodenough, J.B.: Metallic oxides. Prog. Solid State Chem. **5**, 145 (1971)
41. Dimitrijevic, N.M., Savic, D., Micic, O.I., Nozik, A.J.: Interfacial electron-transfer equilibria and flat-band potentials of alpha-Fe_2O_3 and TiO_2 colloids studied by pulse-radiolysis. J. Phys. Chem. **88**, 4278 (1984)
42. Nakau, T.: Electrical Conductivity of α-Fe_2O_3. J. Phys. Soc. Jpn. **15**, 727 (1960). doi:10.1143/JPSJ.15.727
43. Benjelloun, D., Bonnet, J.P., Doumerc, J.P., Launay, J.C., Onillon, M., Hagenmuller, P.: Anisotropy of the electrical-properties of iron-oxide alpha-Fe_2O_3. Mater. Chem. Phys. **10**, 503 (1984)
44. Rosso, K.M., Smith, D.M.A., Dupuis, M.: An ab initio model of electron transport in hematite (alpha-Fe_2O_3) basal planes. J. Chem. Phys. **118**, 6455 (2003). doi:10.1063/1.1558534
45. Shinar, R., Kennedy, J.H.: Photoactivity of doped alpha-Fe_2O_3 electrodes. Solar Energy Mater. **6**, 323 (1982)
46. Leygraf, C., Hendewerk, M., Somorjai, G.: The preparation and selected properties of Mg-doped para-type iron-oxide as a photo-cathode for the photoelectrolysis of water using visible-light. J. Solid State Chem. **48**, 357 (1983)
47. Sastri, M.V.C., Nagasubramanian, G.: Studies on ferric oxide electrodes for the photo-assisted electrolysis of water. Int. J. Hydrogen Energy **7**, 873 (1982)
48. Maruska, H.P., Ghosh, A.K.: Transition-metal dopants for extending the response of titanate photoelectrolysis anodes. Solar Energy Mater. **1**, 237 (1979)
49. Butler, M.A.: Photoelectrolysis and physical-properties of semiconducting electrode WO_3. J. Appl. Phys. **48**, 1914 (1977)
50. Hardee, K.L., Bard, A.J.: Semiconductor electrodes 5. Application of chemically vapor-deposited iron-oxide films to photosensitized electrolysis. J. Electrochem. Soc. **123**, 1024 (1976)
51. Yeh, L.S.R., Hackerman, N.: Iron-oxide semiconductor electrodes in photoassisted electrolysis of water. J. Electrochem. Soc. **124**, 833 (1977)
52. Quinn, R.K., Nasby, R.D., Baughman, R.J.: Photoassisted electrolysis of water using single-crystal alpha-Fe_2O_3 anodes. Mater. Res. Bull. **11**, 1011 (1976)
53. Sanchez, C., Sieber, K.D., Somorjai, G.A.: The photoelectrochemistry of niobium doped alpha-Fe_2O_3. J. Electroanal. Chem. **252**, 269 (1988)
54. Itoh, K., Bockris, J.O.: Stacked thin-film photoelectrode using iron-oxide. J. Appl. Phys. **56**, 874 (1984)
55. Itoh, K., Bockris, J.O.: Thin-film photoelectrochemistry – iron-oxide. J. Electrochem. Soc. **131**, 1266 (1984)
56. Gärtner, W.W.: Depletion-layer photoeffects in semiconductors. Phys. Rev. **116**, 84 (1959)
57. Alexander, B.D., Kulesza, P.J., Rutkowska, L., Solarska, R., Augustynski, J.: Metal oxide photoanodes for solar hydrogen production. J. Mater. Chem. **18**, 2298 (2008). doi:10.1039/b718644d
58. Van de Krol, R., Liang, Y.Q., Schoonman, J.: Solar hydrogen production with nanostructured metal oxides. J. Mater. Chem. **18**, 2311 (2008). doi:10.1039/b718969a
59. Sapieszko, R.S., Matijevic, E.: Preparation of well-defined colloidal particles by thermal-decomposition of metal-chelates. 1. Iron-oxides. J. Colloid Interface Sci. **74**, 405 (1980)
60. Moser, J., Grätzel, M.: Photoelectrochemistry with colloidal semiconductors – laser studies of halide oxidation in colloidal dispersions of TiO_2 and alpha-Fe_2O_3. Helv. Chim. Acta **65**, 1436 (1982)

61. Stramel, R.D., Thomas, J.K.: Photochemistry of iron-oxide colloids. J. Colloid Interface Sci. **110**, 121 (1986)
62. Kiwi, J., Grätzel, M.: Light-induced hydrogen formation and photo-uptake of oxygen in colloidal suspensions of alpha-Fe_2O_3. J. Chem. Soc. Faraday Trans. **83**, 1101 (1987)
63. Chatterjee, S., Sarkar, S., Bhattacharyya, S.N.: Size effect in the photochemical generation of hydrogen from water by colloidal Fe_2O_3 particles. J. Photochem. Photobiol. A **72**, 183 (1993)
64. Zeng, S.Y., Tang, K.B., Li, T.W., Liang, Z.H., Wang, D., Wang, Y.K., Qi, Y.X., Zhou, W.W.: Facile route for the fabrication of porous hematite nanoflowers: Its synthesis, growth mechanism, application in the lithium ion battery, and magnetic and photocatalytic properties. J. Phys. Chem. C **112**, 4836 (2008). doi:10.1021/jp0768773
65. Lian, S.Y., Wang, E.B., Gao, L., Wu, D., Song, Y.L., Xu, L.: Surfactant-assisted solvothermal preparation of submicrometer-sized hollow hematite particles and their photocatalytic activity. Mater. Res. Bull. **41**, 1192 (2006). doi:10.1016/j.materresbull.2005.10.022
66. Hu, X.L., Yu, J.C.: Continuous aspect-ratio tuning and fine shape control of monodisperse alpha-Fe_2O_3 nanocrystals by a programmed microwave-hydrothermal method. Adv. Funct. Mater. **18**, 880 (2008). doi:10.1002/adfm.200700671
67. Björksten, U., Moser, J., Grätzel, M.: Photoelectrochemical studies on nanocrystalline hematite films. Chem. Mater. **6**, 858 (1994)
68. Qian, X., Zhang, X., Bai, Y., Li, T., Tang, X., Wang, E., Dong, S.: Photoelectrochemical characteristics of alpha-Fe_2O_3 nanocrystalline semiconductor thin film. J. Nanopart. Res. **2**, 191 (2000)
69. Gou, X.L., Wang, G.X., Kong, X.Y., Wexler, D., Horvat, J., Yang, J., Park, J.: Flutelike porous hematite nanorods and branched nanostructures: Synthesis, characterisation and application for gas-sensing. Chem. Eur. J. **14**, 5996 (2008). doi:10.1002/chem.200701705
70. Hu, X.L., Yu, J.C., Gong, J.M., Li, Q., Li, G.S.: Alpha-Fe_2O_3 nanorings prepared by a microwave-assisted hydrothermal process and their sensing properties. Adv. Mater. **19**, 2324 (2007). doi:10.1002/adma.200602176
71. Hida, Y., Kozuka, H.: Photoanodic properties of sol-gel-derived iron oxide thin films with embedded gold nanoparticles: effects of polyvinylpyrrolidone in coating solutions. Thin Solid Films **476**, 264 (2005). doi:10.1016/j.tsf.2004.09.063
72. Watanabe, A., Kozuka, H.: Photoanodic properties of sol-gel-derived Fe_2O_3 thin films containing dispersed gold and silver particles. J. Phys. Chem. B **107**, 12713 (2003). doi:10.1021/jp0303568
73. Borse, P.H., Jun, H., Choi, S.H., Hong, S.J., Lee, J.S.: Phase and photoelectrochemical behavior of solution-processed Fe_2O_3 nanocrystals for oxidation of water under solar light. Appl. Phys. Lett. **93** (2008). doi:173103 10.1063/1.3005557
74. Souza, F.L., Lopes, K.P., Nascente, P.A.P., Leite, E.R.: Nanostructured hematite thin films produced by spin-coating deposition solution: application in water splitting. Sol. Energy Mater. Sol. Cells **93**, 362 (2009). doi:10.1016/j.solmat.2008.11.049
75. Yue, W.B., Zhou, W.Z.: Crystalline mesoporous metal oxide. Prog. Nat. Sci. **18**, 1329 (2008). doi:10.1016/j.pnsc.2008.05.010
76. Jiao, F., Harrison, A., Jumas, J.C., Chadwick, A.V., Kockelmann, W., Bruce, P.G.: Ordered mesoporous Fe_2O_3 with crystalline walls. J. Am. Chem. Soc. **128**, 5468 (2006). doi:10.1021/ja0584774
77. Vayssieres, L., Beermann, N., Lindquist, S.E., Hagfeldt, A.: Controlled aqueous chemical growth of oriented three-dimensional crystalline nanorod arrays: application to iron(III) oxides. Chem. Mater. **13**, 233 (2001)
78. Fan, Z.Y., Wen, X.G., Yang, S.H., Lu, J.G.: Controlled p- and n-type doping of Fe_2O_3 nanobelt field effect transistors. Appl. Phys. Lett. **87**, 013113 (2005). doi:10.1063/1.1977203
79. Lindgren, T., Wang, H.L., Beermann, N., Vayssieres, L., Hagfeldt, A., Lindquist, S.E.: Aqueous photoelectrochemistry of hematite nanorod array. Sol. Energy Mater. Sol. Cells **71**, 231 (2002)

80. Peng, L.L., Xie, T.F., Fan, Z.Y., Zhao, Q.D., Wang, D.J., Zheng, D.: Surface photovoltage characterization of an oriented alpha-Fe_2O_3 nanorod array. Chem. Phys. Lett. **459**, 159 (2008). doi:10.1016/j.cplett.2008.05.036
81. Fu, Y.Y., Chen, J., Zhang, H.: Synthesis of Fe_2O_3 nanowires by oxidation of iron. Chem. Phys. Lett. **350**, 491 (2001)
82. Wang, R.M., Chen, Y.F., Fu, Y.Y., Zhang, H., Kisielowski, C.: Bicrystalline hematite nanowires. J. Phys. Chem. B **109**, 12245 (2005). doi:10.1021/jp051197q
83. Wen, X.G., Wang, S.H., Ding, Y., Wang, Z.L., Yang, S.H.: Controlled growth of large-area, uniform, vertically aligned arrays of alpha-Fe_2O_3 nanobelts and nanowires. J. Phys. Chem. B **109**, 215 (2005). doi:10.1021/jp0461448
84. Yu, T., Zhu, Y.W., Xu, X.J., Yeong, K.S., Shen, Z.X., Chen, P., Lim, C.T., Thong, J.T.L., Sow, C.H.: Substrate-friendly synthesis of metal oxide nanostructures using a hotplate. Small **2**, 80 (2006). doi:10.1002/smll.200500234
85. Han, Q., Xu, Y.Y., Fu, Y.Y., Zhang, H., Wang, R.M., Wang, T.M., Chen, Z.Y.: Defects and growing mechanisms of alpha-Fe_2O_3 nanowires. Chem. Phys. Lett. **431**, 100 (2006). doi:10.1016/j.cplett.2006.09.027
86. Mor, G.K., Shankar, K., Paulose, M., Varghese, O.K., Grimes, C.A.: Enhanced photocleavage of water using titania nanotube arrays. Nano Lett. **5**, 191 (2005). doi:10.1021/nl048301k
87. Prakasam, H.E., Varghese, O.K., Paulose, M., Mor, G.K., Grimes, C.A.: Synthesis and photoelectrochemical properties of nanoporous iron (III) oxide by potentiostatic anodization. Nanotechnol. **17**, 4285 (2006). doi:10.1088/0957-4484/17/17/001
88. Rangaraju, R.R., Panday, A., Raja, K.S., Misra, M.: Nanostructured anodic iron oxide film as photoanode for water oxidation. J. Phys. D: Appl. Phys. **42**, 135303 (2009). doi:10.1088/0022-3727/42/13/135303
89. Mor, G.K., Prakasam, H.E., Varghese, O.K., Shankar, K., Grimes, C.A.: Vertically oriented Ti-Fe-O nanotube array films: toward a useful material architecture for solar spectrum water photoelectrolysis. Nano Lett. **7**, 2356 (2007). doi:10.1021/nl0710046
90. Mohapatra, S.K., John, S.E., Banerjee, S., Misra, M.: Water photooxidation by smooth and ultrathin α-Fe_2O_3 nanotube arrays. Chem. Mater. **21**, 3048 (2009)
91. Hu, Y.S., Kleiman-Shwarsctein, A., Forman, A.J., Hazen, D., Park, J.N., McFarland, E.W.: Pt-doped alpha-Fe_2O_3 thin films active for photoelectrochemical water splitting. Chem. Mater. **20**, 3803 (2008). doi:10.1021/cm800144q
92. Spray, R.L., Choi, K.-S.: Photoactivity of transparent nanocrystalline Fe_2O_3 electrodes prepared via anodic electrodeposition. Chem. Mater. **21**, 3701 (2009)
93. Murthy, A.S.N., Reddy, K.S.: Photoelectrochemical behavior of undoped ferric-oxide (alpha-Fe_2O_3) electrodes prepared by spray pyrolysis. Mater. Res. Bull. **19**, 241 (1984)
94. Duret, A., Grätzel, M.: Visible light-induced water oxidation on mesoscopic alpha-Fe_2O_3 films made by ultrasonic spray pyrolysis. J. Phys. Chem. B **109**, 17184 (2005). doi:10.1021/jp044127c
95. Kumari, S., Tripathi, C., Singh, A.P., Chauhan, D., Shrivastav, R., Dass, S., Satsangi, V.R.: Characterization of Zn-doped hematite thin films for photoelectrochemical splitting of water. Curr. Sci. **91**, 1062 (2006)
96. Liang, Y.Q., Enache, C.S., Van de Krol, R.: Photoelectrochemical characterization of sprayed alpha-Fe_2O_3 thin films: influence of Si doping and SnO_2 interfacial layer. Int. J. Photoenergy 739864 (2008). doi:10.1155/2008/739864
97. Satsangi, V.R., Kumari, S., Singh, A.P., Shrivastav, R., Dass, S.: International Workshop on Hydrogen Energy – Production Storage and Application, Jaipur, India, 2006
98. Khan, S.U.M., Akikusa, J.: Photoelectrochemical splitting of water at nanocrystalline n-Fe_2O_3 thin-film electrodes. J. Phys. Chem. B **103**, 7184 (1999)
99. Hagglund, C., Grätzel, M., Kasemo, B.: Comment on "Efficient photochemical water splitting by a chemically modified n-TiO_2" – (II). Science **301**, 1673B (2003)

100. Sartoretti, C.J., Alexander, B.D., Solarska, R., Rutkowska, W.A., Augustynski, J., Cerny, R.: Photoelectrochemical oxidation of water at transparent ferric oxide film electrodes. J. Phys. Chem. B **109**, 13685 (2005)
101. Cesar, I.: Thesis results, Chimie et Génie Chimique Ecole Polytechnique Fédérale de Lausanne, Lausanne (2007)
102. Cesar, I., Kay, A., Martinez, J.A.G., Grätzel, M.: Translucent thin film Fe_2O_3 photoanodes for efficient water splitting by sunlight: Nanostructure-directing effect of Si-doping. J. Am. Chem. Soc. **128**, 4582 (2006). doi:10.1021/ja060292p
103. Orthner, H.R., Roth, P.: Formation of iron oxide powder in a hot-wall flow reactor – effect of process conditions on powder characteristics. Mater. Chem. Phys. **78**, 453 (2002)
104. Wen, J.Z., Goldsmith, C.F., Ashcraft, R.W., Green, W.H.: Detailed kinetic modeling of iron nanoparticle synthesis from the decomposition of $Fe(CO)_5$. J. Phys. Chem. C **111**, 5677 (2007). doi:10.1021/jp066579q
105. Kay, A., Cesar, I., Grätzel, M.: New benchmark for water photooxidation by nanostructured alpha-Fe_2O_3 films. J. Am. Chem. Soc. **128**, 15714 (2006). doi:10.1021/ja064380l
106. Glasscock, J.A., Barnes, P.R.F., Plumb, I.C., Savvides, N.: Enhancement of photoelectrochemical hydrogen production from hematite thin films by the introduction of Ti and Si. J. Phys. Chem. C **111**, 16477 (2007). doi:10.1021/jp0745561
107. Saretni-Yarahmadi, S., Wijayantha, K.G.U., Tahir, A.A., Vaidhyanathan, B.: Nanostructured alpha-Fe_2O_3 electrodes for solar driven water splitting: effect of doping agents on preparation and performance. J. Phys. Chem. C **113**, 4768 (2009). doi:10.1021/jp808453z
108. Saremi-Yarahmadi, S., Tahir, A.A., Vaidhyanathan, B., Wijayantha, K.G.U.: Fabrication of nanostructured alpha-Fe_2O_3 electrodes using ferrocene for solar hydrogen generation. Mater. Lett. **63**, 523 (2009). doi:10.1016/j.matlet.2008.11.011
109. Grätzel, M.: Mesoscopic solar cells for electricity and hydrogen production from sunlight. Chem. Lett. **34**, 8 (2005). doi:10.1246/Cl.2005.8
110. Ernst, K., Belaidi, A., Konenkamp, R.: Solar cell with extremely thin absorber on highly structured substrate. Semicond. Sci. Technol. **18**, 475 (2003)
111. Grätzel, M., Augustynski, J.: Tandem cell for water cleavage by visable light. (2000). PCT Int. Appl., WO 2001002624 (2001)
112. Brillet, J., Cornuz, M., Le Formal, F., Yum, J.H., Grätzel, M., Sivula, K.: Examining architectures of photoanode-photovoltaic tandem cells for solar water splitting. J. Mater. Res. **25**, 17 (2010). doi:10.1557/JMR.2010.0009
113. Hu, Y.S., Kleiman-Shwarsctein, A., Stucky, G.D., McFarland, E.W.: Improved photoelectrochemical performance of Ti-doped alpha-Fe_2O_3 thin films by surface modification with fluoride. Chem. Commun. **19**, 2652 (2009). doi:10.1039/b901135h
114. Brunschwig, B.S., Chou, M.H., Creutz, C., Ghosh, P., Sutin, N.: Mechanisms of water oxidation to oxygen – cobalt(IV) as an intermediate in the aquocobalt(II)-catalyzed reaction. J. Am. Chem. Soc. **105**, 4832 (1983)
115. Kanan, M.W., Nocera, D.G.: In situ formation of an oxygen-evolving catalyst in neutral water containing phosphate and Co^{2+}. Science **321**, 1072 (2008). doi:10.1126/science.1162018
116. Zhong, D.K., Sun, J.W., Inumaru, H., Gamelin, D.R.: Solar water oxidation by composite catalyst/alpha-Fe_2O_3 photoanodes. J. Am. Chem. Soc. **131**, 6086 (2009). doi:10.1021/ja9016478
117. Eggleston, C.M., Shankle, A.J.A., Moyer, A.J., Cesar, I., Grätzel, M.: Anisotropic photocatalytic properties of hematite. Aquat. Sci. **71**, 151 (2009). doi:10.1007/s00027-009-9191-5
118. Yanina, S.V., Rosso, K.M.: Linked reactivity at mineral–water interfaces through bulk crystal conduction. Science **320**, 218 (2008). doi:10.1126/science.1154833
119. Gualtieri, A.F., Venturelli, P.: In situ study of the goethite-hematite phase transformation by real time synchrotron powder diffraction. Am. Mineral. **84**, 895 (1999)

120. Pailhe, N., Wattiaux, A., Gaudon, M., Demourgues, A.: Impact of structural features on pigment properties of alpha-Fe_2O_3 haematite. J. Solid State Chem. **181**, 2697 (2008). doi:10.1016/j.jssc.2008.06.049
121. Chernyshova, I.V., Hochella, M.F., Madden, A.S.: Size-dependent structural transformations of hematite nanoparticles. 1. Phase transition. Phys. Chem. Chem. Phys. **9**, 1736 (2007). doi:10.1039/b618790k
122. Woodhouse, M., Parkinson, B.A.: Combinatorial discovery and optimization of a complex oxide with water photoelectrolysis activity. Chem. Mater. **20**, 2495 (2008)
123. Woodhouse, M., Parkinson, B.A.: Combinatorial approaches for the identification and optimization of oxide semiconductors for efficient solar photoelectrolysis. Chem. Soc. Rev. **38**, 197 (2009). doi:10.1039/b719545c
124. Jang, J.S., Lee, J., Ye, H., Fan, F.R.F., Bard, A.J.: Rapid screening of effective dopants for Fe_2O_3 photocatalysts with scanning electrochemical microscopy and investigation of their photoelectrochemical properties. J. Phys. Chem. C **113**, 6719 (2009). doi:10.1021/jp8109429
125. Sivula, K., Le Formal, F., Grätzel, M.: Solar Water Splitting: Progress Using Hematite (α-Fe_2O_3) Photoelectrodes. Chemsuschem **4**, 432 (2011). doi: 10.1002/cssc.201000416